Retrieval of aerosol component directly from satellite and ground-based measurements

Lei Li[1,2], Oleg Dubovik[2*], Yevgeny Derimian[2*], Gregory L Schuster[3], Tatyana Lapyonok[2], Pavel Litvinov[4], Fabrice Ducos[2], David Fuertes[4], Cheng Chen[2], Zhengqiang Li[5], Anton Lopatin[4], Benjamin Torres[2] , Huizheng Che[1]

[1]State Key Laboratory of Severe Weather (LASW) and Key Laboratory of Atmospheric Chemistry (LAC), Chinese Academy of Meteorological Sciences, CMA, Beijing, 100081, China
[2]Univ. Lille, CNRS, UMR 8518 - LOA - Laboratoire d'Optique Atmosphérique, F-59000 Lille, France
[3]NASA Langley Research Center, Hampton, VA, USA
[4]GRASP-SAS, Remote Sensing Developments, Cité Scientifique, Univ. Lille, Villeneuve d'Ascq, 59655, France
[5]State Environmental Protection Key Laboratory of Satellite Remote Sensing, Institute of Remote Sensing and Digital Earth, Chinese Academy of Sciences, Beijing 100101, China

Correspondence to:
O. Dubovik (oleg.dubovik@univ-lille.fr);
Y. Derimian (yevgeny.derimian@univ-lille.fr)

Abstract

This study presents a novel methodology for remote monitoring of aerosol components over large spatial and temporal domains. The concept is realized within the GRASP (Generalized Retrieval of Aerosol and Surface Properties) algorithm to directly infer aerosol components from the measured radiances. The observed aerosols are assumed to be mixtures of hydrated soluble particles embedded with black carbon, brown carbon, iron oxide, and other (non-absorbing) insoluble inclusions. The complex refractive indices of the dry components are fixed a priori (although the refractive index of the soluble host is allowed to vary with hydration), and the complex refractive indices of the mixture are computed using mixing rules. The volume fractions of these components are derived together with the size distribution and the fraction of spherical particles, plus the spectral surface reflectance in cases when the satellite data is inverted. The retrieval is implemented as a

44 statistically optimized fit in a continuous space of solutions. This contrasts with most
45 conventional approaches where the type of aerosol is either associated with a pre-
46 assumed aerosol model that is included in a set of Look-Up-Tables, or determined
47 from the analysis of the retrieved aerosol optical parameters (e.g., single scattering
48 albedo, refractive index, etc. provided by the AERONET retrieval algorithm); here,
49 we retrieve the aerosol components explicitly. The approach also bridges directly to
50 the quantities used in global chemical transport models. We first tested the approach
51 with synthetic data to estimate the uncertainty, and then applied it to real ground-
52 based AERONET and space-borne POLDER/PARASOL observations; thus, the study
53 presents a first attempt to derive aerosol components from satellite specifically tied to
54 global chemical transport model quantities. Our results indicate aerosol optical
55 characteristics that are highly consistent with standard products (e.g., R of ~ 0.9 for
56 aerosol optical thickness) and demonstrate an ability to separate intrinsic optical
57 properties of fine- and coarse-sized aerosols. We applied our method to
58 POLDER/PARASOL radiances on the global scale and obtained spatial and temporal
59 patterns of the aerosol component that agree well with the knowledge on aerosol
60 sources and transport features. Finally, we discuss limitations and perspectives of this
61 new technique.
62

1 Introduction

64   Information about atmospheric aerosol chemical composition has a great
65 importance for monitoring and understanding of various aspects of climate and
66 environment. This information can be obtained by laboratory analysis of sampled
67 aerosol. However, the in-situ measurements require considerable effort and represent
68 only small geographic areas without providing results on wide spatial and temporal
69 scale. It is known that chemical transport models are able to represent chemical
70 component concentrations with wide spatial and temporal coverage, and this
71 capability has been developed rapidly in the past decade. However, the models can
72 have uncertainties because they are initialized by gridded emission inventories that
73 presently have substantial uncertainties. For example, the carbon emissions
74 inventories can be uncertain with a factor of two, and this uncertainty is carried
75 forward to the model output (Bond et al., 1998; Cooke et al., 1999; Streets et al.,
76 2001).
77   Aerosol components are often divided into two categories: strongly light-absorbing
78 components and mainly scattering (non-absorbing) components. The radiative
79 impacts of aerosols at the top of the atmosphere can change from cooling to warming
80 as their optical properties change from highly scattering to highly absorbing (e.g.
81 Haywood and Shine, 1995). There are two kinds of absorbing aerosols that are
82 commonly found in the atmosphere: absorbing carbon and mineral dust that contains
83 iron oxides (Sokolik and Toon, 1999).
84   Light-absorbing carbon is produced by incomplete combustion, and it is an
85 important component of atmospheric aerosol. The complex refractive index of light-
86 absorbing carbon is dependent upon the type of the fuel and the conditions of

87 combustion (Andreae and Gelencsér, 2006; Schkolnik et al., 2007). The term black
88 carbon (BC) is begrudgingly (and universally) associated with soot carbon in the
89 climate science community, and constitutes the strongest light-absorbing carbon
90 found in the atmosphere (Andreae and Gelencsér, 2006; Bond et al., 2013).
91 Meanwhile, the term brown carbon (BrC) is used to denote organic matter that
92 contains some absorbing organic species, and generally has much greater absorption
93 at near-ultraviolet and blue wavelengths than at red wavelengths (Chen and Bond,
94 2010; Dinar et al., 2007; Hoffer et al., 2006; Jacobson, 1999; Kanakidou et al., 2005;
95 Kirchstetter et al., 2004; Schnaiter et al., 2006; Sun et al., 2007).

96   Mineral dust particles can also have a strong spectral signature, with strong
97 absorption at the UV and blue wavelengths when iron oxides are present. Hematite
98 and goethite are different forms of free iron, and they typically appear together
99 (Arimoto et al., 2002; Formenti et al., 2014; Lafon et al., 2006; Shi et al., 2012). The
100 presence of iron in mineral dust particles is known to be important for its
101 biogeochemical and radiative impacts (Jickells et al., 2005; Mahowald et al., 2005;
102 Sokolik and Toon, 1999). Although the regional distribution of the iron concentration
103 is important for climate studies, it is difficult to obtain since it requires in-situ aerosol
104 sampling or simulation of complex natural processes. In addition, mineral dust
105 particles can be affected by the presence of anthropogenic aerosol particles (e.g.
106 carbonaceous particles produced from biomass burning).

107   Separating the absorption associated with light-absorbing carbon from the
108 absorption associated with mineral dust (especially iron oxides) is not an obvious task
109 (Derimian et al., 2008), and determination of the relative proportions of BC, BrC and
110 iron oxides should consider differences in absorption spectral dependence. For
111 instance, Dubovik et al. (2002a) showed that the spectral absorption of carbonaceous
112 aerosol is distinct from that of mineral dust. Schuster et al. (2005) inferred the BC
113 column content from AERONET retrievals by assuming BC is the source of all
114 significant aerosol absorption in the AERONET retrievals. Koven and Fung (2006)
115 retrieved hematite concentration at dust sites based upon the spectral variability of the
116 imaginary refractive index, while Arola et al. (2011) retrieved BrC from AERONET
117 retrievals. Wang et al. (2013) have added single-scatter albedo as an additional
118 constraint to the approach using refractive index (Arola et al., 2011; Schuster et al.,
119 2005) and made it feasible to distinguish BC, BrC and dust simultaneously. Similarly,
120 Li et al. (2015, 2013) investigate the microphysical, optical and chemical properties of
121 atmospheric aerosols by fitting the AERONET complex refractive indices measured
122 at Beijing and Kanpur. Recently, Schuster et al. (2016a) have used the AERONET
123 size distributions and complex refractive indices to retrieve the relative proportion of
124 carbonaceous aerosols (BC and BrC) and free iron minerals (hematite and goethite) in
125 fine and coarse mode particles. Nevertheless, all of these methods for retrieving
126 aerosol component rely upon an intermediate retrieval of the refractive index and/or
127 the aerosol absorption optical depth (e.g. one provided by the AERONET operational
128 inversion). Importantly, we also note that these retrievals of aerosol components are
129 only conducted for ground-based remote sensing measurements.

130   Global satellite observations of aerosol properties provide an opportunity to
131 validate and constrain the model simulations at large spatial and temporal scales
132 (Collins et al., 2001; Liu et al., 2005; Yu et al., 2006, 2004, 2003; Zhang et al.,
133 2008a). The integration of observations with model results can fill gaps in satellite
134 retrievals and constrain global distributions of aerosol properties to have good
135 agreement with ground-based measurements (Liu et al., 2005; Yu et al., 2006, 2003).
136 In this regard, inverse modeling can be used to reduce large aerosol simulation
137 uncertainties. For instance, several studies (Chen et al., 2018, 2019; Dubovik et al.,
138 2008; Henze et al., 2007) showed the ability to retrieve global aerosol sources with
139 inverse models that rely upon satellite observations. Therefore, the practice of satellite
140 data fusion into models provides a possibility of improving aerosol simulations of the
141 pre- and post-satellite eras. However, besides the knowledge of amounts
142 (concentrations) and locations of aerosol emissions, accurate modeling of atmospheric
143 aerosols and their effects also requires information about particle composition. The
144 lack of comprehensive datasets providing multiple constraints for the key parameters
145 employed in models has hindered the improvement of model simulation. Specifically,
146 improving the ability of aerosol component estimation will require enhancement of
147 remote sensing capabilities to provide the aerosol component information on the
148 global scale. The accuracy and specification of the aerosol components as retrieved
149 from satellite observations should respond to the requirements of the aerosol transport
150 models. At the same time, the information content of remote sensing is limited and
151 the main challenge is to identify the aerosol component parameters that can be
152 successfully retrieved by remote sensing measurements, given their sensitivity to the
153 aerosol optical properties and complex refractive index in particular.

154   The POLDER space instrument (Deschamps et al., 1994; Tanré et al., 2011) is an
155 example of the instrument providing satellite observations that are sensitive to aerosol
156 components. The implementation of multi-wavelength, multi-angle and polarization
157 measurement capabilities has made it possible to derive particle properties (size,
158 shape and absorption; Dubovik et al., 2011; Waquet et al., 2013) that are essential for
159 characterizing and estimating aerosol components. This study presents a methodology
160 for the direct retrieval of aerosol components from such measurements. Our
161 methodology is stimulated by the Schuster et al. (2016a, 2009, 2005) works on
162 deriving aerosol component information from ground-based Sun/sky photometers of
163 the AERONET network. Here, the idea has evolved and expanded to retrieving the
164 aerosol components from satellite remote sensing observations as well. Namely, we
165 have incorporated an aerosol component module into the Generalized Retrieval of
166 Aerosol and Surface Properties (GRASP) algorithm (Dubovik et al., 2014, 2011). It
167 should be noted that GRASP is a versatile algorithm designed to retrieve an extended
168 set of atmospheric parameters from diverse remote sensing data, including surface,
169 airborne, and satellite observations. Here, we apply GRASP to both ground- and
170 space-based observations, with a primary objective of developing an approach for
171 monitoring aerosol components with extensive spatial and temporal coverage.

172   The objective of our GRASP/Component approach is to retrieve the aerosol
173 components directly from remote sensing measurements without intermediate

retrieval of the complex refractive index, as in previous studies (Arola et al., 2011; Koven and Fung, 2006; Li et al., 2015, 2013; Schuster et al., 2016a, 2009, 2005; Wang et al., 2013). This new approach has a more direct link to the measured radiance field than the "intermediate" approaches, and we therefore expect a reduction in the retrieval uncertainties. The GRASP/Component approach also incorporates an additional constraint on the refractive index spectral variability that is not employed in the conventional retrieval algorithms. Specifically the spectral variability of aerosol complex refractive index is constrained in the GRASP/Component retrieval by the spectral dependences of the aerosol species used in the algorithm. It is expected that such constraints can improve the retrievals in various situations.

One of the principal difficulties, however, is the identification of an adequate conversion model for linking refractive index to aerosol component. An ideal conversion model should cover the entire range of aerosol complex refractive indices and also provide a unique connection between spectral refractive index and aerosol component. Therefore, our primary objective focuses on identifying the optimal transformation of chemical and physical aerosol information to optical properties (e.g. refractive index). Once developed, the efficiency of the concept is verified and demonstrated by applying GRASP/Component to ground-based Sun/sky photometric measurements, since this type of measurement usually presents a higher sensitivity to aerosol absorption than satellite remote sensing. Finally, the outcome of the GRASP/Component approach is demonstrated with the application of the aerosol component retrieval to multi-angular polarimetric POLDER/PARASOL satellite observations.

It should be noted that the retrieval of aerosol type has been clearly recognized as an important task by the scientific community and has been addressed in several studies. For example, there are a number of approaches that attempt to identify the type of aerosol through analysis of optical parameters such as single scattering albedo (SSA), Ångström Exponent (AE), AAE (absorption AE), refractive index, etc. Specifically, Russell et al. (2014) relate AERONET- and POLDER-derived optical properties to different aerosol types: urban, dust, marine, biomass burning, etc. Studies by Chung et al. (2010) and Bahadur et al. (2012) use AERONET optical properties like AE and AAE to separate BC, BrC, and dust into species-specific AAOT (absorption AOT). Schuster et al. (2005, 2009, 2016a) and Li et al. (2015) quantify the relative volume fractions of one or more aerosol species (e.g. BC, BrC, iron oxide, water) by adjusting the mixture of several components in an aerosol model to fit AERONET-retrieved refractive indices. However, our new approach differs substantially from all of these methods because it does not use a retrieval of optical parameters as an intermediate step. Thus, we expect the GRASP/Component approach to provide a stronger link to the radiation field than the previous approaches, as well as fundamentally higher retrieval accuracy.

Moreover, some of above methods have additional differences and limitations compared to our proposed approach. For example, the Russell et al. (2014) approach is rather qualitative and does not attempt to quantify the relative volume or mass

fractions of different species in an aerosol mixture. Chung et al. (2012) and Bahadur et al. (2012) seem to use a technique for separating carbonaceous aerosols from dust that is not fully consistent with the AERONET retrieval assumptions, as discussed by Schuster et al. (2016b).

Also, the Look-Up Table (LUT) approaches employed in most satellite retrievals (Martonchik et al., 1998; Remer et al., 2005; Kahn and Gaitley, 2015; Popp et al., 2016; Hammer et al., 2018; etc.) are designed to search amongst a preselected set of aerosol models (or their mixtures) for a model that provides the best fit to the observations. Since the models in a LUT are usually associated with a number of aerosol types (e.g. desert dust, smoke, urban aerosol etc.), the identification of the model that provides the best fit is often considered as a retrieval of aerosol type/composition. For observations with enhanced sensitivity, such as the Multi-angle Imaging SpectroRadiometer (MISR), a large number of models can be justified in the LUT and the differentiation of the models described by the ensembles of parameters can indeed be rather robust. However, LUT approaches are fundamentally limited to a discrete set of possible solutions, whereas the GRASP/Component approach searches through a continuous space of solutions; thus, the identification of aerosol components with our new methodology is significantly more detailed and elaborate. The proposed approach also bridges directly to the quantities of aerosol compositions used in the global chemical transport models. Specifically, our aerosol component retrievals can satisfy the requirements of chemical transport models (CTM) to constrain their aerosol estimations on a large or global scale. The proposed methodology eliminates two intermediate steps commonly used in comparing satellite results with models. First, the retrieval is done directly from measured radiances to components without passing through retrieved optical properties or assume aerosol models. Second, the methodology allows matching CTM components without passing through often ambiguous AOT to mass conversions, e.g. using like mass extinction efficiency. However, we note that the GRASP/Component approach is only possible if 1) there is significant instrument sensitivity to the parameters that are related to aerosol component (i.e. complex refractive index), and 2) this sensitivity is maintained while other parameters such as the size distribution are adjusted.

2 Methodology

GRASP is a highly rigorous and versatile aerosol and surface reflectance retrieval algorithm that is accessible at https://www.grasp-open.com (Dubovik et al., 2014, 2011). It was demonstrated that GRASP algorithm can provide retrieval of rather complete set of aerosol parameters from multi-angular satellite polarimetry or AERONET like ground-based observations. The set of retrieved parameters includes size distribution, complex refractive index, information about particle shape, as well as, various optical properties as AOT, single scattering albedo, Ångström Exponent, etc. The values of these parameters certainly are related to aerosol type, however, they do not provide any direct information about possible aerosol type or quantitative

261 indication of various components presence in the observed aerosol. The identification
262 of presenting aerosol types can be obtained by matching the retrieved parameters into
263 preselected the basis of aerosol components with known properties (e.g., Russell et
264 al., 2014). However, such approach relies on several intermediate steps based of the
265 assumptions of rather different methodological nature and therefore each step
266 introduces additional uncertainties and even ambiguity. The essence of
267 methodological developments in this study is to develop an approach of retrieving
268 directly aerosol components from observations with no intermediate steps and
269 uniquely set assumptions.

270 The central point of technical developments in this study is to integrate a new
271 conversion model designed to link aerosol component with optical and microphysical
272 characteristics into the standard GRASP inversion procedure. The general logistics is
273 shown in Fig. 1 (modified from (Dubovik et al., 2011)). The algorithm is divided into
274 several interacting but rather independent modules to enhance its flexibility. The
275 straightforward exchange of limited parameters minimizes the interactions between
276 the modules. The "Forward Model" and "Numerical Inversion" are the two most
277 complex and elaborate modules in the algorithm. The "Forward Model" is developed
278 in a quite universal way to quantitatively simulate the measured atmospheric radiation
279 with given surface and aerosol properties. The "Numerical Inversion" module (which
280 can be used in various applications, some not even related to atmospheric remote
281 sensing) includes general mathematical operations unrelated to the particular physical
282 nature of the observations. Numerical inversion is implemented as a statistically
283 optimized fitting of observations based upon the multi-term least squares method
284 (LSM), and combines the advantages of a variety of approaches. The module provides
285 transparency and flexibility for developing algorithms that invert passive or active
286 observations to derive several groups of unknown parameters (Dubovik, 2004).

287 As a consequence of such organization of the algorithm, it can equally be applied
288 (with minimal changes) to invert observations from different satellite sensors or
289 ground-based instruments (Benavent-oltra et al., 2017; Espinosa et al., 2017; Lopatin
290 et al., 2013; Román et al., 2018, 2017; Tsekeri et al., 2017). A full description of the
291 "Forward Model" and "Numerical Inversion" algorithm modules can be found in
292 Dubovik et al. (2011). The following sections provide a description of the
293 modifications conducted for realization of the GRASP/Component approach
294 (schematically presented by red dashed frames in Fig. 1).

295

296 2.1 Forward model

297

298 The formulation of the forward radiative transfer modeling in the presented
299 approach is generally similar to the formulation of the standard GRASP algorithm
300 where the modeling of the aerosol scattering matrices has been implemented
301 following the ideas described in Dubovik and King (2000) and Dubovik et al. (2006,
302 2002b). However, we implemented some modifications in modeling of aerosol single
303 scattering. Namely, the real and imaginary parts of the aerosol complex refractive

304   index are calculated using fractions of aerosol components and fixed refractive index
305   of these elements as assumed in the conversion model. Thus, the new component
306   approach uses the same forward model as described in Dubovik et al. (2011), except
307   that aerosol component fractions are iterated in the vector of the retrieved unknowns
308   (instead of refractive index) and refractive index is computed a posteriori.

309   It is worth noting that the aerosol properties in the GRASP algorithm are retrieved
310   simultaneously with the surface reflectance characteristics. The land surface
311   Bidirectional Reflectance Distribution Function (BRDF) in GRASP is described by
312   the kernel-driven Ross-Li model. This model uses a linear combination of three
313   kernels f_{iso}, f_{vol}, and f_{geom} representing isotropic, volumetric, and geometric optics
314   surface scattering, respectively (Li and Strahler, 1992; Roujean et al., 1992; Wanner
315   et al., 1995). The semi-empirical equation by Maignan et al. (2009) is used for the
316   Bidirectional Polarization Distribution Function (BPDF). The reflective properties of
317   ocean surface are modeled analogously to earlier POLDER algorithm developments
318   (Deuzé et al., 2001; Herman et al., 2005; Tanré et al., 2011). Fresnel reflection of the
319   agitated sea surface is taken into account using the Cox and Munk model (Cox and
320   Munk, 1954). The water leaving radiance is nearly isotropic (Voss et al., 2007) and
321   modeling shows that its polarization is negligible (Chami et al., 2001; Chowdhary et
322   al., 2006; Ota et al., 2010). The Fresnel term and the white cap reflection are taken
323   into account by Lambertian unpolarized reflectance. The whitecap reflectance is
324   driven by the wind speed at the sea surface according to the Koepke model (Koepke,
325   1984). The seawater reflectance at short wavelengths depends on the properties of
326   oceanic water and can be significant. Thus, in present model, the wind speed and the
327   magnitude of seawater reflectance at each wavelength are retrieved simultaneously
328   with the atmospheric aerosol properties.

329   The aerosol and surface characteristics are determined by parameters included in
330   the vector of unknowns and correspondingly they are inferred from observations.
331   Table 1 shows the list of measurements and retrieved parameters from
332   POLDER/PARASOL observations. For AERONET retrieval the list of parameters is
333   not shown here. However, in principle, it is analogous to POLDER/PARASOL, with
334   the difference that the set of observations is different (i.e. AERONET uses AOT and
335   transmitted total radiances at different wavelengths) and that surface parameters are
336   not retrieved but fixed from the climatology.

337

2.2 Numerical inversion

339   The numerical inversion implemented in this study follows the methodology
340   described in the paper of Dubovik et al. (2011). The only difference is that the
341   GRASP/Component approach retrieves the fractions of different aerosol components
342   instead of the spectral dependence of the complex refractive index. Therefore, this
343   section describes only the modifications that are needed to implement the
344   GRASP/Component approach.

345   GRASP retrieval is designed as a statistically optimized fitting routine and uses
346   multiple a priori constraints. GRASP can implement two different scenarios of

347 satellite retrievals: (i) conventional single-pixel retrieval for processing of satellite
348 images pixel by pixel and (ii) multiple-pixel retrieval for inverting a large group of
349 pixels simultaneously. The multi-pixel approach can be used for
350 POLDER/PARASOL data for improving consistency of temporal and spatial
351 variability of retrieved characteristic. The main modifications required for the
352 component approach are related to the definition of a priori constraints.
353 Correspondingly, two types of a priori constraints are reformulated in the component
354 retrieval approach: constraints for single pixel and constraints limiting inter-pixel
355 variability of derived parameters.

356 **2.2.1 Single-pixel observation fitting**

357 For each i-th pixel, the retrieval follows a multi-term LSM fitting of joint sets of
358 data combining the observations with a priori constraints defined by the system of
359 equations $\boldsymbol{f}_i^* = \boldsymbol{f}_i(\boldsymbol{a}_i) + \Delta\boldsymbol{f}_i$:

360

361
$$\begin{cases} \boldsymbol{f}_i^* = \boldsymbol{f}_i(\boldsymbol{a}) + \Delta\boldsymbol{f}_i \\ 0_i^* = \boldsymbol{S}_i\boldsymbol{a}_i + \Delta(\Delta\boldsymbol{a}_i) \Rightarrow \boldsymbol{f}_i^* = \boldsymbol{f}_i(\boldsymbol{a}_i) + \Delta\boldsymbol{f}_i \\ \boldsymbol{a}_i^* = \boldsymbol{a}_i + \Delta\boldsymbol{a}_i^* \end{cases} \tag{1}$$

362

363 Here, the term with a star represents satellite measurements. For example, $\boldsymbol{f}_i^*$
364 denotes a vector of the measurements, $\boldsymbol{f}_i$ denotes a vector of the estimations, $\Delta\boldsymbol{f}_i$
365 denotes a vector of measurement uncertainties, $\boldsymbol{a}_i$ denotes a vector of unknowns in i-
366 th pixel. The second expression in Eq. (1) characterizes the a priori smoothness
367 assumptions that constrain the variability of the size distributions and the spectral
368 dependencies of the retrieved surface reflectance parameters. The matrix S includes
369 the coefficients for calculating the m-th differences of $dV(r_j)/dlnr$, $Frac(i)$,
370 $f_{iso}(\lambda_i)$, $f_{vol}(\lambda_i)$, and $f_{geom}(\lambda_i)$. $Frac(i)$ denotes the fraction of component,
371 $dV(r_j)/dlnr$ $(i = 1, ..., N_r)$ denotes the values of volume size distribution in N_i size
372 bins r_i normalized by C_v and $f_{iso}(\lambda_i)$, $f_{vol}(\lambda_i)$, $f_{geom}(\lambda_i)$ characterize the property
373 of surface reflectance in the Ross-Li model. The m-th differences are numerical
374 equivalents of the m-th derivatives. 0_i^* represents vector of zeros and $\Delta(\Delta\boldsymbol{a})$
375 represents vector of the uncertainties that characterizes the deviations of the
376 differences from the zeros. This equation indicates that all of these m-th differences
377 are equal to zeros within the uncertainties $\Delta(\Delta\boldsymbol{a}_i)$. The third expression in Eq. (1)
378 includes the vector of a priori estimates $\boldsymbol{a}_i^*$, as well as the vector of the uncertainties
379 $(\Delta\boldsymbol{a}_i^*)$ in a priori estimates of the i-th pixel.
380 The statistically optimized solution of Eq. (1) corresponds to the minimum of the
381 following quadratic form (according to multi-term LSM):

382

383
$$\Psi_i(\boldsymbol{a}_i) = \Psi_f(\boldsymbol{a}_i) + \Psi_\Delta(\boldsymbol{a}_i) + \Psi_a(\boldsymbol{a}_i)$$

384
$$= \tfrac{1}{2}((\Delta\boldsymbol{f}^P)^T(\boldsymbol{W}_f)^{-1}\Delta\boldsymbol{f}^P + \gamma_\Delta(\boldsymbol{a}_i)^T\Omega\boldsymbol{a}_i + \gamma_a(\boldsymbol{a}_i - \boldsymbol{a}_i^*)^T\boldsymbol{W}_a^{-1}(\boldsymbol{a}_i - \boldsymbol{a}_i^*)). \tag{2}$$

385

386 Following Dubovik et al. (2011), all equations are expressed with weighting
387 matrices W that are defined as $W = (1/\varepsilon^2)C$ (dividing the corresponding covariance
388 matrix C by its first diagonal element ε^2); the Lagrange multipliers γ_a and γ_Δ are
389 written as $\gamma_\Delta = \varepsilon_f^2/\varepsilon_\Delta^2$ and $\gamma_a = \varepsilon_f^2/\varepsilon_a^2$, where $\varepsilon_f^2, \varepsilon_\Delta^2$, and ε_a^2 represent the first
390 diagonal elements of corresponding covariance matrices C_f, C_Δ, and C_a. Thus, in this
391 general formulation the fractions ($Frac(i)$) of aerosol component are presented as
392 unknowns instead of $n(\lambda_j)$ and $k(\lambda_j)$.

393

394 2.2.2 Multiple-pixel observation fitting

395 In this retrieval regime the fitting for a group of pixels is constrained by the extra a
396 priori limitations on inter-pixel variability of aerosol and/or surface reflectance
397 properties. Since the information content of the reflected radiation from a single pixel
398 is sometimes insufficient for a unique retrieval of all unknown parameters, the
399 presented approach can improve the stability of satellite data inversions (Dubovik et
400 al., 2011). The inversion of the multi-pixel observations is a solution for a combined
401 system of equations. For example, a three-pixel system can be defined as following:

402

403
$$
\begin{cases}
f_1^* = f_1(a_1) + \Delta f_1 \\
f_2^* = f_2(a_2) + \Delta f_2 \\
f_3^* = f_3(a_3) + \Delta f_3 \\
\quad\quad \dots \\
0_x^* = S_x a + \Delta(\Delta_x a) \\
0_y^* = S_y a + \Delta(\Delta_y a) \\
0_t^* = S_t a + \Delta(\Delta_t a)
\end{cases}
, \tag{3}
$$

404
405 where the subscript "i" (i=1, 2, 3, …) is the pixel index. The total vector of unknowns
406 a is combined by the vectors of unknowns a_i of each i-th pixel, i.e. $a^T =$
407 $(a_1; a_2; a_3)^T$. The matrices S_x, S_y and S_t include the coefficients for calculating the
408 m-th differences of spatial or temporal inter-pixel variability for each retrieved
409 parameter a_k that characterizes $dV(r_j)/dlnr$, $Frac(i)$, $f_{iso}(\lambda_i)$, $f_{vol}(\lambda_i)$, and
410 $f_{geom}(\lambda_i)$. The vectors $0_x^*, 0_y^*, 0_t^*$ denote vectors of zeros and the vectors $\Delta(\Delta_x a)$,
411 $\Delta(\Delta_y a)$ and $\Delta(\Delta_t a)$ denote vectors of the uncertainties characterizing the deviations
412 of the differences from the zeros.
413 The statistically optimized multi-term LSM solution corresponds to the minimum
414 of the following quadratic $\Psi(a^P)$:

415

416
$$
\Psi(a^P) = \left(\sum_{i=1}^{Npixels} \Psi_i(a^P) \right) + \frac{1}{2}(a^P)^T \Omega_{inter} a^P. \tag{4}
$$

417 This is the sum of the corresponding single-pixel forms (first term) and an inter-pixel
418 smoothing component (2nd term). The smoothness matrix Ω_{inter} in the inter-pixel
419 smoothing term is defined as:

420

421
$$
\Omega_{inter} = \gamma_x S_x^T S_x + \gamma_y S_y^T S_y + \gamma_t S_t^T S_t. \tag{5}
$$

422

423 Hence, the solution of a multi-pixel system of N pixels is not equivalent to the
424 solution of N independent single pixel systems.

425

2.2.3 A priori smoothness constraints of fitting

426

427   For the framework of deriving aerosol component from the POLDER/GRASP
428 retrieval, the vector $\boldsymbol{a}_i$ is composed as:

429

430
$$\boldsymbol{a} = (\boldsymbol{a}_v \boldsymbol{a}_{frac} \boldsymbol{a}_{sph} \boldsymbol{a}_{Vc} \boldsymbol{a}_h \boldsymbol{a}_{brdf,1} \boldsymbol{a}_{brdf,2} \boldsymbol{a}_{brdf,3} \boldsymbol{a}_{bpdf})^T, \tag{6}$$

431

432 where $\boldsymbol{a}_v$, $\boldsymbol{a}_{frac}$, and $\boldsymbol{a}_{sph}$ represent the constituents of the vector a corresponding to
433 $dV(r_i)/dlnr$, $Frac(i)$ and C_{sph} (denotes the fraction of spherical particles). Then $\boldsymbol{a}_h$
434 characterizes the mean altitude of the aerosol layer h_a, the element $\boldsymbol{a}_{Vc}$ represents the
435 total volume concentration, and $\boldsymbol{a}_v$ are the logarithms of $dV(r)/dlnr$ which are
436 normalized by total volume concentration. The three components
437 $(\boldsymbol{a}_{brdf,1}, \boldsymbol{a}_{brdf,2}, \boldsymbol{a}_{brdf,3})$ are related to the logarithms of the spectrally dependent
438 parameters $k_{iso}(\lambda_i)$, $k_{vol}(\lambda_i)$ and $k_{geom}(\lambda_i)$ employed in Ross-Li model. The vector
439 $\boldsymbol{a}_{bpdf}$ includes the parameters of the BPDF model. Thus, this work differentiates
440 from Dubovik et al. (2011) by retrieving the volume fractions of the aerosol
441 components (i.e. $Frac(i)$) instead of the complex refractive index.
442   There is no evident connection between the retrieved fractions of aerosol
443 component in each single pixel, so no smoothness constraints are used for $\boldsymbol{a}_{frac}$. The
444 matrix S for each i-th pixel is the same and has the following array structure (Dubovik
445 et al., 2011):

446

447
$$\boldsymbol{Sa} = \begin{pmatrix} S_v & 0 & 0 & 0 & 0 & 0 & 0 & 0 & 0 \\ 0 & 0 & 0 & 0 & 0 & 0 & 0 & 0 & 0 \\ 0 & 0 & 0 & 0 & 0 & 0 & 0 & 0 & 0 \\ 0 & 0 & 0 & 0 & 0 & 0 & 0 & 0 & 0 \\ 0 & 0 & 0 & 0 & 0 & 0 & 0 & 0 & 0 \\ 0 & 0 & 0 & 0 & S_{brdf,1} & 0 & 0 & 0 & 0 \\ 0 & 0 & 0 & 0 & 0 & S_{brdf,2} & 0 & 0 & 0 \\ 0 & 0 & 0 & 0 & 0 & 0 & S_{brdf,3} & 0 & 0 \\ 0 & 0 & 0 & 0 & 0 & 0 & 0 & S_{bpdf} & \end{pmatrix} \begin{pmatrix} \boldsymbol{a}_v \\ a_{frac} \\ a_{sph} \\ a_{Vc} \\ a_h \\ \boldsymbol{a}_{brdf,1} \\ \boldsymbol{a}_{brdf,2} \\ \boldsymbol{a}_{brdf,3} \\ \boldsymbol{a}_{bpdf} \end{pmatrix}, \tag{7}$$

448

449 where the corresponding matrices $S_{...}$ have different dimensions and describe
450 differences of different order. The vectors in Eq. (7) corresponding to $\boldsymbol{a}_{frac}$, $\boldsymbol{a}_{sph}$,
451 $\boldsymbol{a}_{Vc}$, $\boldsymbol{a}_h$ contain only zeros because no smoothness constraint can be applied to these
452 parameters. The errors $\Delta(\Delta\boldsymbol{a})$ are assumed independent for different components of
453 the vector $(\Delta\boldsymbol{a})^*$ and the smoothness matrix for each i-th pixel can be written as:

454

455
$$\gamma_\Delta \Omega = \begin{pmatrix} \gamma_{\Delta,1}\Omega_1 & 0000 & 0 & 0 & 0 & 0 \\ 0 & 0000 & 0 & 0 & 0 & 0 \\ 0 & 0000 & 0 & 0 & 0 & 0 \\ 0 & 0000 & 0 & 0 & 0 & 0 \\ 0 & 0000 & 0 & 0 & 0 & 0 \\ 0 & 0000 & \gamma_{\Delta,2}\Omega_2 & 0 & 0 & 0 \\ 0 & 0000 & 0 & \gamma_{\Delta,3}\Omega_3 & 0 & 0 \\ 0 & 0000 & 0 & 0 & \gamma_{\Delta,4}\Omega_4 & 0 \\ 0 & 0000 & 0 & 0 & 0 & \gamma_{\Delta,5}\Omega_5 \end{pmatrix}, \tag{8}$$

456

457 where $\Omega_i = S_i^T W_i^{-1} S_i$ (i=1, …, 5), S_v, $S_{brdf,1}$, $S_{brdf,2}$,

458 $S_{brdf,3}$, S_{bpdf}.

459   The inter-pixel smoothing term given by Eq. (5) is defined in a very similar way as

460 described by Dubovik et al. (2011), and therefore it is not written here explicitly.

461 Indeed, the spatial and temporal variability of component is very similar to the

462 variability of refractive index, since both depend only upon the variability of aerosol

463 type.

464   We note that the above equations apply to the POLDER/GRASP retrievals, but

465 corresponding equations are trivially obtained for the AERONET/GRASP retrievals

466 by excluding parameters describing surface reflectance and aerosol height.

467

468

2.3 Model of optical properties of aerosol component

469

2.3.1 Definition and assumptions

470

471   The aerosol refractive index required for the forward calculations (see Fig. 1) is

472 derived by assuming a mixing model and employing fractions of aerosol species;

473 therefore, the retrieval of aerosol component requires the selection of a mixing rule. In

474 our work, we decided to use a simple and widely tested Maxwell-Garnett effective

475 medium approximation. Indeed, the choice of the mixing rule is of importance since it

476 can affect the retrieval results. For example, the study of Xie et al. (2014) showed that

477 the Bruggeman approximation was found as more suitable for the dust case, the

478 Maxwell-Garnett for the haze case, and volume average for the clean case. Thus, in

479 order to get an idea about the influence of the mixing rule choice, in our study the

480 retrievals were produced also using the volume weighted mixing rule. We have not

481 identified a significant influence of the mixing rule choice on the quality of the

482 retrievals in our approach. Moreover, the aerosol optical properties were rather well

483 comparable in both cases. The fractions of the elements evidently present some

484 differences due to the differences in the formulation, but are still in a reasonable

485 agreement.

486   The Maxwell-Garnett mixing rule has been extensively applied in many studies for

487 retrieval of aerosol component from ground-based remote sensing measurements (Li

488 et al., 2015, 2013; Schuster et al., 2016a, 2009, 2005; Wang et al., 2013). As Fig. 2

489 illustrates, the first step in the Maxwell-Garnett conversion model is the designation

of a "host" and calculation of the refractive index of the host. In general, the host can be formed by water and soluble inorganic species (e.g. ammonium nitrite, ammonium sulfate, sea salt). It is well known that inorganic salt particles are mostly hygroscopic and deliquescence in humid air. The phase transition from a solid particle to a saline droplet (host) usually occurs when the relative humidity reaches a specific value, known as the deliquescence point, that is specific to the chemical composition of the aerosol particle (Orr et al., 1958; Tang, 1976; Tang and Munkelwitz, 1993). The refractive indices of hygroscopic aerosols change with the additional amount of water that is absorbed in response to changing relative humidity. These changes in refractive index, including also the changes in specific density, size and mass fraction, have been accurately measured as functions of relative humidity (Tang, 1996; Tang and Munkelwitz, 1994, 1991). Schuster et al. (2009) illustrated that the soluble aerosol components (sea salt, ammonium sulfate, ammonium nitrate, etc.) indicate similar refractive indices for similar mixing ratios, even though the dry refractive indices can be quite different. Hence, the aerosol water fraction can be derived from the mixture real refractive index if the aerosols are known to be one of the common soluble aerosols.

In the presented approach, the host is assumed to depend upon the properties and proportions of ammonium nitrate and water (uncertainties due to selection of ammonium nitrate are evaluated further on). The real refractive index (at the 0.6328 μm wavelength) for a host mixture of ammonium nitrate and water can be expressed as

$$n = 1.33 + (1.22 \times 10^{-3})X + (8.997 \times 10^{-7})X^2 + (1.666 \times 10^{-8})X^3, \qquad (9)$$

where X is the weight percent of ammonium nitrate (Tang and Munkelwitz, 1991).

Refractive indices at other wavelengths are spectrally interpolated utilizing measured data (Downing and Williams, 1975; Gosse et al., 1997; Hale and Querry, 1973; Kou et al., 1993; Palmer and Williams, 1974; Tang, 1996; Tang and Munkelwitz, 1991). A detailed description and FORTRAN subroutines for calculating the host complex refractive index is accessible at the website of GACP (Global Aerosol Climatology Project, https://gacp.giss.nasa.gov/data_sets/).

Once the refractive index of the host is determined, the refractive index of the mixture is computed using the Maxwell-Garnett equations. The Maxwell-Garnett effective medium approximation allows computation of the average dielectric function based upon the average electric fields and polarizations of a host matrix with embedded inclusions, and can model insoluble particles suspended in a solution (Bohren and Huffman, 1983; Lesins et al., 2002).

The dielectric functions of aerosols are not typically tabulated in the literature, so they must be computed from the refractive index. Once the dielectric functions are known for the host and its constituents, the Maxwell-Garnett dielectric function for a mixture can be calculated. For example, for two types of inclusions in a host, the dielectric function of the mixture can be expressed as (Schuster et al., 2005):

534
$$\varepsilon_{MG} = \varepsilon_m \left[1 + \frac{3(f_1 \frac{\varepsilon_1 - \varepsilon_m}{\varepsilon_1 + 2\varepsilon_m} + f_2 \frac{\varepsilon_2 - \varepsilon_m}{\varepsilon_2 + 2\varepsilon_m})}{1 - f_1 \frac{\varepsilon_1 - \varepsilon_m}{\varepsilon_1 + 2\varepsilon_m} - f_2 \frac{\varepsilon_2 - \varepsilon_m}{\varepsilon_2 + 2\varepsilon_m}} \right], \tag{10}$$

535

536   where ϵ_m, ϵ_1, and ϵ_2 are the complex dielectric functions of the host matrix and
537   inclusions, and f_1, f_2 are the volume fractions of the inclusions. If we use the case of
538    $f_2 = 0$, the corresponding complex refractive index of the mixture can be obtained by
539   Eqs. (11) and (12):

540
$$m_r = \sqrt{\frac{\sqrt{\varepsilon_r^2 + \varepsilon_i^2} + \varepsilon_r}{2}}, \tag{11}$$

541

542
$$m_i = \sqrt{\frac{\sqrt{\varepsilon_r^2 + \varepsilon_i^2} - \varepsilon_r}{2}}, \tag{12}$$

543

544   where ε_r and ε_i denote the real and imaginary components of the mixture dielectric
545   function, ε_{MG}.

546   The selected refractive indices of inclusions in the Maxwell-Garnett effective
547   medium approximation model in this study are shown in Fig. 3. Figure 3 also
548   illustrates the assumption on the size resolved aerosol components presented as an
549   additional constraint. Table 2 shows the description of aerosol components and the
550   complex refractive indices at 0.440 μm and 0.865 μm of each component employed
551   in the GRASP/Component approach, as well as those used in the uncertainty tests.
552   Our selection of aerosol elements and the size resolved component results from the
553   examination of a series of sensitivity tests and stability of the inversion results. The
554   size resolved component formulation was chosen because a similarity in spectral
555   signatures of some aerosol species induced a difficulty of their distinguishing in the
556   considered in this study observational configuration. For instance, brown carbon
557   (BrC) and iron oxides (hematite and goethite) have similar tendency in spectral
558   absorption; that is, increasing the imaginary refractive index towards ultraviolet
559   wavelengths (Chen and Cahan, 1981; Chen and Bond, 2010; Kerker et al., 1979;
560   Schuster et al., 2016a). At the same time, it is known that carbonaceous absorbing
561   aerosol particles dominate in the fine mode and mineral dust absorption dominates in
562   the coarse mode. Hence, black carbon (BC) and brown carbon (BrC) are assumed to
563   be the only absorbing insolubles in the fine mode and iron oxides are assumed to be
564   the only absorbing insolubles in the coarse mode. In addition, the fine mode includes
565   non-absorbing insoluble species (FNAI) that represent fine dust or non-absorbing
566   organic carbon (OC), non-absorbing soluble species (FNAS) representing
567   anthropogenic salts and aerosol water content (FAWC). The coarse mode includes
568   absorbing insoluble species (CAI), which are mainly iron oxides, but can also include
569   all other absorbing elements. The coarse mode also includes non-absorbing insoluble
570   (CNAI) species that mainly represent the bulk dust material, but can be also non-
571   absorbing insoluble organic carbon particles, non-absorbing soluble species (CNAS)

representing anthropogenic or natural salts (e.g. sea salts) and aerosol water content (CAWC). It should be clarified that refractive index of only one element is used for each species; however, our tests confirmed that some elements are indistinguishable from the optical point of view, at least for the measurement configurations expected in the scope of the presented algorithm applications. Thus, several of the assumed species in the mixing model elements can be associated with different elements. It should be also mentioned that the maximal fractions for BC and CAI (mainly representing iron oxides) are limited in the algorithm due to possible range of complex refractive indices in the pre-computed kernels of aerosol optical characteristics. That is, the volume fractions of these two highly absorbing species are limited in the algorithm to 10% for BC and 3% for CAI. The limitation criteria are based on previous in-situ studies (Ganor and Foner, 1996; Guieu et al., 2002; Lafon et al., 2004, 2006, Alfaro et al., 2004; Wagner et al., 2012; Formenti et al., 2014) demonstrating that the volume fraction of free iron in dust particles approximately accounts for 1.4 – 3.25% (2.8 – 6.5% by mass as the density is 4.28 g cm^{-3} for goethite, 5.25 g cm^{-3} for hematite, and 2.65 g cm^{-3} for illite, kaolinite, quartz, and calcite; Formenti et al., 2014). The fraction of BC in atmospheric aerosol was generally reported not exceeding 10% (Bond et al., 2013). Analysis of our results showed that the introduced maximal values were never reached in the inversion procedure and therefore the presented limitations should not introduce artificially limited concentrations. It is also to note that the retrievals of aerosol component derived from AERONET measurements by Schuster et al. (2016a) demonstrated that the volume fraction of free iron remains relatively constant in West Africa throughout the year (1.4 – 1.7%) and the volume fraction of black carbon reaches a peak of 1.0% for the fine mode during West African biomass burning season and a peak of 3.0% for the fine mode in southern Africa biomass burning.

2.3.2 Sensitivity tests

Using the above modifications to the GRASP algorithm described in Dubovik et al. (2011), the aerosol component retrieval approach was tested for inversion of ground-based AERONET and POLDER/PARASOL satellite observations. For verification of the proposed concept and the algorithm performance, a series of sensitivity tests were conducted using synthetic data. The overall strategy of these tests, as well as of analysis of obtained results below in the paper, was, first, to demonstrate and verify that GRASP/Component approach matches the standard GRASP retrievals in terms of AOT, AE and SSA under the predefined component divisions. Then, second, if this match is achieved, to demonstrate the possibility of unique distinction of component in sensitivity tests and to verify agreement with available independent data of the retrieved results.

A comprehensive series of sensitivity tests were mainly conducted with the POLDER/PARASOL observations because, unlike the AERONET retrievals, sensitivity of POLDER/PARASOL observations to aerosol complex refractive index

614 has not been systematically explored. Thus, first, the POLDER/PARASOL radiances
615 and polarization measurements were simulated using forward calculations. Then, the
616 synthetic measurements were inverted using the GRASP algorithm with the size-
617 dependent aerosol component approach and the Maxwell-Garnett mixing model. The
618 tests were conducted for a range of aerosol component fractions for the species
619 described above and a variety of observational configurations such as spectral
620 channels, viewing geometry etc. Figure 4 presents an example of the assumed and
621 retrieved fractions of aerosol species in fine and coarse modes. The statistics of the
622 sensitivity test results are presented in Table 3, where we compare assumed and
623 retrieved aerosol parameters (fractions of aerosol elements, aerosol optical thickness
624 (AOT), Single Scattering Albedo (SSA) and complex refractive index at 675 nm).
625 The results for other wavelengths are very similar to that presented at 675 nm. In all
626 the conducted tests, the results demonstrated that in frame of the designed model the
627 use of the size-dependent Maxwell-Garnett conversion model allows the algorithm to
628 distinguish amongst the assumed aerosol species, including ammonium nitrate and
629 water in the host.

630

2.3.3 Uncertainty assessment
631

632 An important range of variability exists in the literature-reported refractive indices
633 of the aerosol species. Different assumptions on the refractive index of an aerosol
634 species can result in different retrieved fractions of the species proposed in this study.
635 To evaluate a possible range of the retrieved fractions due to uncertain knowledge of
636 the refractive indexes and difficulty to select one representative value, a series of
637 supplementary calculations were conducted using a range of refractive indices found
638 in the literature. Figure 5 shows the refractive indices employed in the algorithm and
639 those used for the assessment of the uncertainties in the retrieved aerosol fractions.
640 The uncertainty is defined in percentage as the retrieved fraction minus the assumed
641 fraction and divided by the assumed fraction. The tests are conducted as follows: first,
642 synthetic measurements are created by forward calculations while employing the
643 complex refractive index assumed in the algorithm; second, another complex
644 refractive index is used in the inversion procedure while retrieving the fractions of the
645 aerosol species from the synthetic measurements. Thus, the comparison of the
646 assumed in the forward calculations and the retrieved in the inversion procedure
647 aerosol species fractions provides an error assessment due to possible variability of
648 their complex refractive index. The calculations were conducted for all aerosol
649 species that are assumed be embedded in the host of the Maxwell-Garnett effective
650 medium approximation. In addition, the tests are also conducted for different fractions
651 of the elements and for different values of AOT, reflecting sensitivity of the retrievals
652 to varying aerosol loading.
653 An extensive review of BC refractive indices can be found in Bond and Bergstrom
654 (2006) where the recommended imaginary part is in range from 0.63 to 0.79 at visible
655 wavelengths. The spectrally invariant value of 0.79 was adopted in the previous

656 studies (Bond et al., 2013; Bond and Bergstrom, 2006). Based on this literature, we
657 use the spectrally invariant complex refractive index for BC of 1.95 + 0.79i for our
658 current aerosol component retrievals. We estimate then the uncertainty in the
659 retrieved BC fraction using a BC refractive index of 1.75 + 0.63i. The results of the
660 uncertainty test for retrieving BC from POLDER/PARASOL are presented in Fig. 6a.
661 As can be seen, the uncertainty strongly depends on the BC fraction and increases
662 when the BC fractions are low. We note that the uncertainty can be large (over 100
663 %) when the BC fraction is below 0.01 and aerosol loading is weak. However, the
664 uncertainty decreases rapidly and can be 50 % or better for moderate and high aerosol
665 loading (AOT at 440 nm equal or more than 0.4) and when the BC fraction is above
666 0.01. Therefore, the estimates should be quite reasonable in the cases of large
667 pollution loading.

668 The reported in the literature refractive index of BrC is variable. For the forward
669 model we employed the BrC refractive index derived from Sun et al. (2007), which
670 was used to retrieve aerosol component from ground-based remote sensing
671 measurements (e.g. Arola et al., 2011; Schuster et al., 2016a). The BrC refractive
672 index, representing carbonaceous particles with light absorption in the blue and
673 ultraviolet spectral regions emitted from biomass combustion (Kirchstetter et al.,
674 2004), was used for the uncertainty estimate. The tests show (Fig. 6b) that the
675 uncertainty in BrC fraction is more than 100 % when the fractions are below 0.1 and
676 decreases to below 100 % when the BrC fractions are above 0.1 and the aerosol
677 loading is elevated. Note that the uncertainty in BrC fraction is within 50 % when the
678 fractions are above 0.1 even for very low aerosol loading (AOT = 0.05).

679 Hematite and goethite are the dominant absorbers in the coarse mode particles. The
680 hematite refractive index was selected for the employed aerosol component mixing
681 model. The literature shows that the hematite refractive indices can also exhibit quite
682 a large range of variability (e.g. see Fig. 5b). Figure 6c thus shows the uncertainties in
683 the retrieved CAI fraction from POLDER/PARASOL associated with the hematite
684 refractive given by Longtin et al. (1988) in the forward calculations and of Triaud
685 (2005) in the inversion. Except the very low fraction of CAI (below 0.005), the
686 uncertainty in CAI fraction is within 50 %.

687 The insoluble organic carbon and the non-absorbing dust present very similar
688 spectral dependence of complex refractive index (Ghosh, 1999; Koepke et al., 1997)
689 and it is practically impossible to distinguish between these species in the considered
690 in this work measurement configurations and the retrieval approach. Thus, the non-
691 absorbing insoluble organic carbon and non-absorbing mineral dust are expressed by
692 a non-absorbing insoluble species (NAI). The refractive index for the NAI in the
693 presented algorithm was taken as the dust refractive index in Ghosh (1999). The
694 uncertainty tests for the NAI fraction retrievals are presented for fine and coarse
695 fractions by replacing the dust refractive index with the refractive indices of dust
696 composed of quartz (Ghosh, 1999), kaolinite (Sokolik and Toon, 1999) and illite
697 (Sokolik and Toon, 1999) with the proportions of 48%, 26%, and 26%, respectively
698 (the proportions are recalculated from (Journet et al., 2014)) (see legend of Fig. 5).
699 The estimated uncertainties for fine and coarse NAI fractions (FNAI and CNAI)

700 decrease significantly (from 100 % to below 50 % and varying about the zero) when
701 the NAI fraction is above 0.1 (see Fig. 7a and 7b).

702 The non-absorbing insoluble component can represent not only non-absorbing
703 dust, but also non-absorbing organic carbon, as was mentioned above. Thus, an
704 additional test was conducted when the dust refractive index (Ghosh, 1999) used in
705 the forward calculations was replaced at the retrievals stage by refractive index of
706 insoluble organic carbon from Koepke et al. (1997). The corresponding results of the
707 retrieved in this case fine and coarse fractions of NAI for POLDER/PARASOL
708 observations are presented in Fig. 7c and 7d. The variability for each fraction
709 indicates that the choice of NAI refractive index can cause an uncertainty in the
710 retrieved NAI fraction less than 100% for FNAI and less than 50% for CNAI when
711 the fractions are above 0.1.

712 Figure 8 shows the uncertainties for the host species fraction (FNAS, CNAS,
713 FAWC, and CAWC), which are attributed to the differences between the refractive
714 indices and hygroscopic properties of ammonium nitrate and ammonium sulfate. The
715 uncertainties are small for FNAS, CNAS, FAWC, and CAWC, particularly when the
716 fractions are more than 0.2.

717
718

3 Application to real remote sensing data

3.1 Component retrieval from AERONET

721 AERONET provides measurements that are among the most sensitive data to the
722 aerosol refractive index. In addition, the AOT in AERONET is result of direct
723 measurements and not retrieved as in the case of satellite observations. The GRASP
724 aerosol component retrieval concept was therefore first tested with the real
725 AERONET data to check if the retrieved optical characteristics are consistent with the
726 results of standard AERONET product.

727 Figure 9 presents the AERONET measured AOT and Ångström Exponent (870
728 nm/440 nm) and retrieved Single-Scattering Albedo (SSA) at 675 nm versus those
729 retrieved using the GRASP/Component approach. Namely, the operational
730 AERONET product is presented versus the derived from GRASP/Component for 3
731 sites in the African continent: Banizoumbou (data for April 2007), Skukuza (data for
732 September 2007), and Ilorin (data for January 2007), representing according to the
733 sites location and the considered seasons the dust, the biomass burning and the
734 mixture of dust and biomass burning cases, respectively. It can be seen that the
735 aerosol optical properties are reproduced very well by GRASP/Component approach
736 not only for the recalculated AOT and its spectral behavior, but also for the SSA. The
737 mean difference in AOT is about 0.01, which is on the level of the AERONET
738 calibration uncertainty, the difference in SSA is also well within the expected retrieval
739 uncertainty of 0.03 (Dubovik et al., 2002a). There is no biases observed and the
740 correlation coefficient is nearly 1.0 for AOT and Ångström Exponent.

741   It should be mentioned here that the fine mode in the presented retrievals is
742 described by 10 bins and the coarse mode by 15 bins, which is different than the 22
743 bins that are used for the entire size distribution in the standard AERONET algorithm
744 (Fig. 9). The component retrieval has the ability to infer different refractive indices
745 for the fine and coarse modes. This is a significant improvement over the standard
746 AERONET and POLDER/PARASOL algorithms, which allow refractive indices to
747 vary with wavelength but not with size. Indeed, the use of fixed spectral dependences
748 of the refractive indices in the GRASP/Component algorithm provides an additional
749 constraint and reduces the number of the unknown parameters. Thus, this approach
750 makes the inversion more stable. Nevertheless, the inter-comparison of retrievals by
751 the component approach shows full consistency with the operational AERONET
752 product, mainly thanks to an additional physical constraint on the spectral dependence
753 of refractive index.

754   In addition to the better characterization of aerosol fine and coarse modes and
755 preserving consistency in retrievals of optical characteristics, the new approach can
756 also provide insights on aerosol components. For example, Fig. 10 shows the volume
757 fractions of aerosol species retrieved in fine and coarse modes (panels a-f), and
758 fractions of the species in the total volume (panels g-i) for the mentioned above
759 African sites. The Banizoumbou site is located near Niamey (Niger) north of the
760 Sahel, the Ilorin site (Nigeria) is located in the Sahel, and the Skukuza site is located
761 in southern Africa. The retrieved aerosol components for Banizoumbou and Ilorin
762 present similarity in terms of abundant dust aerosol. However, contributions of BrC
763 and BC are strong in Ilorin, and the contribution of coarse absorbing insoluble aerosol
764 fraction is strong in Banizoumbou. The southern Africa site presents a different
765 picture: a strong contribution of coarse mode soluble and of fine mode non-absorbing
766 insoluble aerosol fractions attributed to water soluble organic carbon and water
767 insoluble organic carbon in the biomass burning region, and almost twice more
768 important than in the Sahel site contribution of BC. The BrC contribution, however, is
769 about two times smaller in southern Africa than that in Sahel, which is consistent with
770 AERONET's low spectral dependence for the imaginary index. The SSA in
771 Banizoumbou is highest (0.97 at 675 nm) and in Skukuza is lowest (0.82) because
772 dust and biomass burning aerosols dominate respectively in these two regions.
773
774
775

776 **3.2 POLDER/PARASOL satellite observations**

777   After testing the aerosol component retrieval approach with the AERONET
778 measurements, the algorithm was applied to the POLDER/PARASOL satellite
779 observations. Figures 11, 12 and Table 4 summarize an inter-comparison of aerosol
780 optical characteristics derived by the GRASP/Component approach applied for
781 POLDER/PARASOL and those of the operational AERONET product. The inter-
782 comparison is presented for six sites in Africa and Middle East (Fig. 11) and for all
783 available AERONET data (Fig. 12) representing performance for different aerosol

784 types and on the global scale. Because of a limited sensitivity to absorption when the
785 aerosol loading is low, the SSA product is filtered for AOT at 0.440 μm equal or
786 higher than 0.4 (Dubovik et al., 2002a; Dubovik and King, 2000). The SSA and the
787 Ångström Exponent in Fig. 11 are presented for all six sites together because the
788 dynamic range of the values for each single site is limited by a dominant aerosol type.
789 It should also be noted that in the inter-comparison on the global scale (Fig. 12) the
790 correlation for Ångström Exponent was notably better for higher AOT (R of ~ 0.6 for
791 all AOTs and of ~ 0.8 for AOT equal or more than 0.2). The better SSA and
792 Ångström Exponent retrievals for higher AOT is, however, known also for standard
793 retrievals and other satellite products (de Leeuw et al., 2015; Popp et al., 2016).
794 Nevertheless, the good agreements for AOT (R is generally of ~ 0.9 or better), and for
795 Ångström Exponent and SSA (R of ~ 0.70 – 0.80) show that the inversion of
796 POLDER/PARASOL satellite measurements using the component approach is
797 consistent with the ground-based AERONET reference in terms of aerosol optical
798 properties. Analysis of the per site aerosol optical properties retrievals for different
799 aerosol types (Fig. 11) also does not reveal any evident problem. In addition, as
800 illustrated in Fig. 13 that the residuals of the GRASP/Component approaches (MG
801 and VW mixing rules) are almost the same as those of standard GRASP. Indeed, the
802 GRASP/Component approaches produce almost the same average residual (2.4 ±
803 0.9% for MG and 2.4 ± 1.0% for VW) as that of the standard GRASP algorithm (2.3
804 ± 0.9%) while the maximum residual for GRASP/Component (5.0% for MG and
805 5.7% for VW) is smaller than that for standard GRASP (6.6%); ± denotes standard
806 deviation.

807 The selected mixing model influence on the retrievals is assessed by comparison of
808 the results from Maxwell-Garnett effective medium approximation with performance
809 using a simplified volume-weighted (VW) aerosol mixture. Definition of the species
810 constituting the VW mixing model is quite similar to Maxwell-Garnett, it employs
811 BC, BrC in fine mode, absorbing insoluble in coarse mode, non-absorbing insoluble
812 and aerosol water content in both fine and coarse modes. The tests were conducted in
813 the same manner as for the Maxwell-Garnett effective medium approximation. The
814 sensitivity tests revealed that implementation of the volume-weighted mixing rule
815 yields stable results and this model can indeed be used for the retrievals. Moreover,
816 the VW model can be preferable in some applications due to its simplicity. Figure 11
817 and Table 4 illustrate that the GRASP/Component retrievals using the MG and VW
818 mixing models almost equally well reproduce the aerosol optical properties. The
819 inter-comparison of the standard GRASP/PARASOL retrievals (without retrieval of
820 aerosol component) with AERONET is also presented in Fig. 11 and Table 4. It
821 should noted that in all three shown cases the results obtained for AOT and Ångström
822 Exponent (AE) from PARASOL using the component approach show comparable and
823 even better correlations with AERONET than the standard GRASP/PARASOL
824 retrieval that derives directly the spectral refractive indices instead of fractions of the
825 aerosol species with fixed refractive indices. This can be considered as confirmation
826 that the constraints adapted in the component approach adequate provide realistic and
827 practically useful additional constraints that help to improve satellite retrievals. At

828   the same time, it can be seen that the SSA obtained by standard GRASP/PARASOL
829   correlates better with AERONET than those obtained by GRASP/PARASOL
830   component approach. Specifically, this GRASP/PARASOL component shows
831   systematically lower absorption than standard GRASP/PARASOL retrieval. This can
832   be explained by the fact that the complex refractive index in GRASP/Component are
833   constrained by the information (on both magnitudes and spectral tendencies) adapted
834   from the literature while in case of standard GRASP/PARASOL and operational
835   AERONET products there are no such constraints. As discussed by Dubovik and
836   King (2000) and Dubovik et al. (2011) the standard retrieval approach uses only
837   smoothness constraints on spectral variability of complex refractive index. In these
838   regards, tests by Dubovik et al. (2000) demonstrated that in presence of measurements
839   noise the standard approach tends to generate retrievals with higher values of
840   absorption in the situation with lower aerosol loading (lower AOT). This happens
841   simply due to increased spread of SSAs for situation with lower aerosol signal.
842   Indeed, due to physical constraints SSA can not higher than 1, as a result appearance
843   of any spread caused by presence of the noise generates lower SSA bias. Such bias
844   has been often discussed by the in situ and modeling community as rather unfortunate
845   feature of AERONET retrievals (e.g., Schmeisser et al., 2017). Therefore, the slightly
846   higher SSA in case of GRASP/Component can be considered rather a positive effect
847   of the additional constrain. Probably, additional focused analysis should be done in
848   future, but it can be expected that the slightly higher values in case of
849   GRASP/Component may also on average be closer to what is expected from models
850   because tied to similar physical assumptions.
851
852

4 Illustration of global scale satellite aerosol component retrieval

855   We processed the POLDER/PARASOL observations globally using the aerosol
856   component retrieval algorithm. The results of this processing present the first attempt
857   to assess the measurement-based global distribution and seasonal variability of
858   aerosol components. The data were processed for the year 2008, which provides a
859   notable variety of different aerosol types, including volcanic aerosols from a
860   Hawaiian eruption.

861   The results are further presented as seasonal means. It should be mentioned
862   however that any interpretation of the statistical values should take into account also
863   the number of available observations. Therefore, it is worth presenting the global
864   maps of the number of available cloud-free pixels. Figure 14 shows that the number
865   of the cloud free pixels over land is significantly higher than over ocean, which can
866   produce a difference in the mean values and create some artificial spatial patterns. In
867   addition, the sensitivity tests and experience of remote sensing observations treatment
868   show that the accuracy of the retrievals is low and the sensitivity to absorbing aerosol
869   and refractive index variability is particularly limited when the aerosol loading is low.

870 Therefore, it is also worth presenting the global maps of the aerosol optical thickness
871 (Fig. 15), prior to analyzing the aerosol component retrievals. It should also be
872 outlined that despite the fractions of the elements are the initial retrieval parameters,
873 direct interpretation of the maps of these fractions can be confusing because do not
874 always correspond to a significant aerosol concentration. For instance, a large fraction
875 of an element retrieved for a size mode where aerosol volume concentration is very
876 low, can have no significant meaning as not having contribution to the optical signal.
877 Therefore, the columnar volume concentrations of the retrieved elements and not the
878 fractions will be further presented. Figures 16 to 21 thus show seasonal variabilities of
879 the retrieved columnar aerosol volume concentrations (mm^3/m^2, which denotes the
880 volume concentration in total atmospheric column with unit surface area) for different
881 aerosol species.

882

883 ## 4.1 Black Carbon

884   The retrieved aerosol component shows patterns of biomass burning in the Sahel
885 and southern Africa regions, expressed by elevated concentrations of BC (Fig. 16).
886 The derived BC concentrations show a pronounced seasonal and spatial variability.
887 The largest concentrations can be observed over the African continent, another
888 noticeable region is Asia, namely India and China. The most intensive BC emissions
889 appear during DJF, which is constituted from contributions of the Sahel region, India
890 and China. Somewhat lower concentrations during SON and JJA are attributed to
891 biomass burning regions in southern African. A global minimum of the BC
892 concentrations is during MAM. The obtained spatial and seasonal patterns of BC are
893 consistent with the knowledge that DJF is the season of intense agricultural burning
894 across the sub-Sahelian region of Africa. BC generated from such agricultural burning
895 can extend for thousands of kilometers from east to west across the continent, as can
896 be seen in Fig. 16. The BC concentration in northern Africa appears mainly over land
897 near the west coast, especially from Senegal south to Gabon on the equator, and over
898 the Gulf of Guinea, which is attributed to the biomass burning during DJF (e.g.
899 Haywood et al., 2008). The BC observed over the ocean is generally transported from
900 biomass burning areas by prevailing trade winds. The retrievals show that the BC
901 concentration in India and China, which can be rather attributed to anthropogenic
902 activity, is maximal during DJF. This result is consistent with a previous study by Li
903 et al. (2015) that also found a maximal BC mass concentration during DJF. The work
904 by Li et al. (2015) is based on retrieval of aerosol component from AERONET
905 measurements in Beijing and Kanpur sites and presents twelve years' climatology for
906 the period 2002 – 2013.

907   During JJA and SON, the elevated BC concentrations are mostly over southern
908 Africa, which is in line with the known African monsoon cycle. The variations of the
909 retrieved BC are consistent with the biomass burning activity progressing from north
910 to south Africa, starting from June, peaking in July - August and then decreasing in

911 intensity until late October with the end of the dry season (Cahoon et al., 1992;
912 Liousse et al., 1996; Maenhaut et al., 1996; Swap et al., 1996).

913 It should be reminded, however, that sensitivity to the absorption and therefore to
914 the BC signal is limited when the AOT is low. In addition, for very low AOT values
915 the aerosol volume concentrations are also low and therefore the retrieved fractions of
916 the aerosol species are more uncertain. Very low aerosol loading is typical for over
917 ocean observations (Fig. 15) and thus appearance of some BC concentrations over
918 ocean should be interpreted with caution.
919

920 **4.2 Brown Carbon**

921 Similar to BC, the observed patterns of BrC (Fig. 17) show seasonal variations,
922 primarily association with the biomass burning in Africa and the contribution of
923 Asian anthropogenic activities. A closer comparison of BrC and BC concentrations
924 reveals, however, that their maximal concentrations are not always collocated. This
925 observation reflects that fresh biomass burning aerosols have higher BC content than
926 aged aerosols (Abel et al., 2003; Haywood et al., 2003; Reid et al., 1998). During
927 SAFARI-2000, for example, the single scattering albedo has an increase from 0.84 to
928 0.90 between smoke close to the source and aged haze 5 h downwind from a large fire
929 (Abel et al., 2003), which is attributed to changes in aerosol component. There can be
930 some rapid changes occurring in the relative concentration of particle types with the
931 aging of smoke and the BC particles become gradually more aggregated with organic
932 and sulfate particles during the aging of smoke (Pósfai et al., 2003). Therefore, the
933 more abundant presence of particles with the spectral absorption signature of BC is
934 reasonable for the areas near the biomass burning emissions, whereas particles with a
935 spectrally dependent absorption signature of BrC are generally enriched in downwind
936 region, which can explain appearance of BrC concentrations in aerosol particles
937 transported over ocean in northern hemisphere.

938

939 **4.3 Fine mode Non-Absorbing Soluble**

940 The NAS component is represented by the real part of the refractive index of
941 ammonium nitrate; however, sulfates, sea salt or aged hydroscopic particles are also
942 included in the NAS component. Figure 18 presents seasonal means of the NAS
943 retrieved for the fine mode (FNAS). The FNAS volume concentration dominates over
944 China and India, especially during DJF and SON, which can correspond to industrial
945 aerosol and heating activity in megacities with high population density. The spatial
946 patterns of FNAS also coincide with the patterns of BC in southern Africa that
947 indicates presence of non-absorbing particles fraction in the biomass burning
948 emissions (e.g. water soluble organic carbon). Indeed, the carbonaceous organic
949 particles can provide a favorable surface for aging processes and sulfate nucleation
950 (Li et al., 2003). Pronounced FNAS particles concentrations are retrieved during JJA
951 over the Mediterranean Sea region, which is in line with the knowledge on abundant

952 presence of anthropogenic and biogenic sulfate particles in the Mediterranean region
953 (Ganor et al., 2000; Lelieveld et al., 2002; Levin, 2005; Levin et al., 1996). The
954 FNAS particles are also retrieved south from the Mediterranean Sea, deep inland over
955 Libya and Egypt. This FNAS component can be possible in this area considering
956 persistent north-south, north-east air mass transport in the eastern Mediterranean
957 region governed by semi-permanent low-pressure trough extending in JJA from the
958 Persian Gulf (Bitan and Sa'Aroni, 1992).
959

4.4 Coarse mode Non-Absorbing Insoluble

961 In the northern and western Africa, the coarse mode non-absorbing insoluble
962 component appears all year long with the pronounced maximum concentrations
963 during MAM to JJA (Fig. 19), representing the non-absorbing part of mineral dust.
964 Notable is a shift in the maximum of this component towards higher latitudes in JJA
965 that corresponds to the northern shift of the inter-tropical convergence zone. The
966 retrievals also clearly show a "hot spot" of coarse mode non-absorbing dust over the
967 Bodélé depression, located between the Tibesti Mountains and Lake Chad, and known
968 as the most active dust source in the Sahara desert (Gasse, 2002; Prospero et al., 2002;
969 Washington et al., 2003). This dust source is caused by the coincidence of an
970 extensive source of diatomite sediment and high velocity winds associated with the
971 Bodélé Low Level Jet (Todd et al., 2007; Washington et al., 2006; Washington and
972 Todd, 2005) with the emission peaks during DJF and MAM (Herrmann et al., 1999;
973 Koren and Kaufman, 2004; Todd et al., 2007; Washington and Todd, 2005) that are
974 also distinguishable in the presented retrievals. This CNAI aerosol type also appears
975 over the Middle East, the Arabian Peninsula and extends over Asia, which is known
976 as the global dust belt. The coarse mode non-absorbing dust concentration is
977 particularly high over the Arabian Peninsula, central to southern Pakistan, as well as
978 over the Oman and Arabian seas. Over this region, the maximum dust concentration is
979 observed during MAM and JJA, while dust concentration substantially decreases
980 during SON and DJF. Higher dust concentration during MAM and JJA is primarily
981 caused by the strong northwesterly winds known as "Shamal Wind" and dry
982 conditions. The JJA peak is caused by several major sources of dust that have
983 maximum dust activity during JJA, including desert areas in Syria and Iraq where a
984 strong northwesterly Shamal Wind is blowing (Choobari et al., 2014). The Sistan
985 region can also be distinguished among the high dust concentrations. This region is
986 considered as a major dust source in southwest Asia (Ginoux et al., 2012; Goudie,
987 2014; Léon and Legrand, 2003; Middleton, 1986a) attributed to the strong persistent
988 northeasterly winds (Alizadeh Choobari et al., 2013; Middleton, 1986b; Miri et al.,
989 2007). This source can cause frequent dust and sand storms, especially during the
990 period of June to August contributing to the deterioration of air quality (Rashki et al.,
991 2013). In addition, during DJF and SON some elevated CNAI concentrations are
992 observed in Australia (area of Lake Eyre and The Great Artesian Basin). It should be
993 also noted that some CNAI concentrations are retrieved during the seasons and over
994 the regions in Africa known for biomass burning and over south-east of USA. These

995 concentrations indicate presence of some coarse mode non-absorbing particles
996 possibly of organic origin.

997

998 4.5 Coarse mode Absorbing Insoluble

999 The Coarse mode Absorbing Insoluble (CAI) particles, which mainly represent the
1000 iron oxides contained in mineral dust, are generally associated with the desert regions
1001 and with the elevated concentrations of CNAI. The high CAI concentrations are
1002 observed during MAM and JJA over western Africa and the Arabian Peninsula (Fig.
1003 20). High CAI concentrations are also retrieved over Asia during the same MAM and
1004 JJA seasons and are quite clearly attributed to the region of the Taklimakan desert
1005 located in northwest China. It is worth noting that the maximum of CAI and CNAI do
1006 not always coincide, reflecting different percentage of iron oxides in desert dust that
1007 is varying depending on the soil mineralogy of the source region. Calculations of the
1008 ratio of CAI to CNAI concentrations over African continent provided values of up to
1009 about 0.05, which is consistent with up to 3 to 5 % iron oxides in desert dust (e.g.
1010 Ganor and Foner, 1996; Guieu et al., 2002; Zhang et al., 2003; Lafon et al., 2004).

1011 The high CAI concentrations over western Africa are mainly present over Niger,
1012 Mauritania and near the west coast. This is in line with a study by Formenti et al.
1013 (2008) that demonstrates the higher iron oxide content in Sahelian dust originated
1014 from the Sahel belt, while a lower content is in the Chad basin. Lázaro et al. (2008)
1015 also reported that the iron oxide content of dust transported to the Canary Islands,
1016 near the west coast, tends to have higher values for source areas between 0°N - 20°N.
1017 In addition, high CAI concentrations are also derived over the Arabian Peninsula and
1018 the Arabian Sea, which may be attributed to the dust originated from Saudi Arabia,
1019 known for presence of an important iron content (Krueger et al., 2004). It should be
1020 mentioned here that a discontinuity in the retrieved concentrations can be noted
1021 between over land and over water in the regions of the Red Sea and Arabian Sea.
1022 Given that such discontinuity does not appear in all coastal regions, but only in
1023 particular circumstances, we suppose that there are some physical explanations. For
1024 instance, the observed discontinuity corresponds well to the land topography, i.e.
1025 presence of surrounding mountains and the observed in other work accumulation of
1026 aerosol over the Red Sea (Brindley et al., 2015). It is also interesting to admit that
1027 some coarse mode absorbing aerosol appear in the regions and seasons associated
1028 with biomass burning and elevated concentrations of BrC and BC in the fine mode,
1029 e.g. in Africa during DJF and SON seasons. This fact can reflect presence of
1030 absorbing carbonaceous material in the coarse mode, which was fitted by refractive
1031 index of iron oxide assumed as only the absorbing component of the coarse mode.

1032

1033 4.6 Fine mode Non-Absorbing Insoluble

1034 Because the fine mode non-absorbing insoluble component (Fig. 21) can stand for
1035 both OC and non-absorbing dust, the Ångström Exponent can be used as an additional

post retrieval criteria for a better interpretation of this component. For instance, the joint FNAI and Ångström Exponent (maps are presented in supplementary material) analysis shows that the particles concentrations derived over western Africa, Middle East, Central Asia and northwest China mainly reflect presence of fine mode non-absorbing dust because are associated with the values of Ångström Exponent generally well below one. Specific examples are the concentrations derived over the Bodélé depression during DJF, the Taklimakan desert in China during MAM and Arabian Peninsula during JJA. However, the elevated FNAI particles concentrations retrieved over southern Africa and South America during JJA and SON, over eastern part of China and Siberia during JJA, and generally over India, are associated with high values of Ångström Exponent, thus should rather be classified as organic carbon. For example, high OC in southern China (Sichuan Basin and the Pearl River Delta region) and urban south Asia is confirmed in several previous studies (Decesari et al., 2010; Stone et al., 2010; Zhang et al., 2008b; Zhang et al., 2012). The OC of urban origin in China is enhanced around May to June and October (Zhang et al., 2012), which may be an explanation of the retrieved high OC concentration during JJA in southern China. Secondary OC (SOC) can also contribute to the total concentrations of OC (Miyazaki et al., 2006; Weber et al., 2007; Zhang et al., 2008b; Zhang et al., 2005) and be retrieved here as FNAI. Additionally, the elevated OC concentration over South America during SON correspond well to the known season of biomass burning that starts in July and peaks generally in August and September (Duncan et al., 2003).

A plume structure of elevated fine non-absorbing insoluble (Fig. 21) and soluble (Fig. 18) components originated from Hawaiian Islands in the North Pacific Ocean is also notable. This structure is visible during three seasons from MAM to SON and corresponds to a Hawaiian volcano emission. The material emitted into the atmosphere in this case was not the coarse volcanic ash, but continuous gaseous emissions that can form secondary aerosol during downwind transport (Craddock and Greeley, 2009; Edmonds et al., 2013). Identification of this material by the suggested approach as a mixture of components equivalent to ammonium sulfate and fine non-absorbing dust is therefore quite plausible.

4.7 Aerosol Water Content and Coarse mode Non-Absorbing Soluble

The algorithm also provides aerosol water content that is required to create the host by mixture with non-absorbing soluble component. As result, the retrieved spatial and temporal patterns of aerosol water content and non-absorbing soluble are very similar. That is, the fine mode aerosol water content is mainly retrieved in the regions with high loading of anthropogenic aerosol, similarly to the fine mode non-absorbing soluble. For instance, the fine mode aerosol water content can be seen over India and China during SON and DJF, at high latitudes of northern hemisphere and over Eurasia during SON. Some notable water concentrations are also retrieved over southern Africa during the biomass burning season (JJA), but mainly over ocean that

1078   correspond to visibly transported and likely aged aerosol. The maps of FAWC are
1079   presented in the supplementary material as they are very similar to already presented
1080   FNAS (Fig. 18).

1081   The retrieved coarse mode aerosol water content and coarse non-absorbing
1082   soluble also present very similar spatial and temporal patterns. However, they are
1083   different from the patterns of fine mode. The concentrations are very low everywhere,
1084   except over ocean in the regions associated with high concentrations of the coarse
1085   non-absorbing insoluble (dust) component. This feature is associated with dust
1086   transported from western Africa and Arabian Peninsula. These coarse mode AWC
1087   and NAS retrievals require a careful interpretation. First, it should be realized that
1088   even relatively small aerosol water fraction retrieved in the regions of very high
1089   aerosol concentration can result in a pronounced volume concentration. In addition,
1090   aerosols with low real refractive index, which cannot be fully explained by the
1091   assumed dust aerosol model, will be interpreted as a water fraction. For instance,
1092   some low water aerosol concentration erroneously appears over the Bodélé depression
1093   during DJF. The Bodélé dust, however, is known to contain much fossil diatom
1094   (Formenti et al., 2008), which would have a different real part of refractive index then
1095   assumed in this study mixture of quartz, kaolinite and illite. At the same time,
1096   possible hygroscopicity of mineral dust, its coating by organics and internal mixture
1097   with sea salt, were found in several laboratory and field studies (e.g. Usher et al.,
1098   2003; Falkovich et al., 2004; Laskin et al., 2005; Derimian et al., 2017). The fact that
1099   the notable aerosol water content is observed in the retrievals only over ocean and not
1100   over land, except for retrievals over Bodélé, also agrees with hypothesis of the dust
1101   hygroscopicity. We therefore conclude that despite this pronounced water aerosol
1102   content in the coarse mode should be questioned and interpreted with caution, a
1103   physical significance of this result should not be excluded. Indeed, this retrieval result
1104   may not be fully understood at present but it was not enforced by any specific
1105   assumption or measurement artifact, and therefore it is likely to represent a
1106   manifestation of specific physical or chemical transformation of aerosol or properties
1107   of dust. In addition to the described above main feature of CAWC and CNAS, the
1108   derived maps are presented in supplements, together with the maps of FAWC, which
1109   are similar to already presented FNAS.

1110

5 Conclusions

1111

1112   We present a new approach for monitoring atmospheric aerosol components with
1113   remote sensing observations. Unlike existing aerosol component retrieval algorithms
1114   that interpret an intermediate retrieval of the refractive index, this study utilizes a
1115   direct fit of measurements. We demonstrate retrievals of several aerosol components
1116   in fine and coarse size modes under assumption of an internal aerosol mixing rule.
1117   The tests using a volume weighted mixing rule were also conducted and the results
1118   compared.

The approach is implemented in a state of the art GRASP algorithm (Dubovik et al., 2014, 2011) designed to process space-borne and ground-based remote sensing observations. The component module is incorporated in GRASP thus the new GRASP/Component version of the code employs mixtures of aerosol components with known refractive indices. This approach serves also as an additional physical constraint on spectral dependences of complex refractive index. The component module uses the Maxwell-Garnett effective medium approximation (EMA) and is based on the Schuster et al. (2016a, 2009) approach, but assumes independent aerosol mixtures in the fine and coarse modes and the direct fit of radiances instead of an intermediate step of fitting the retrieved refractive indices.

A series of numerical sensitivity tests with synthetic data were conducted to evaluate the component retrieval. Results of the tests showed that the new conversion module allows the retrieval to distinguish amongst several assumed aerosol components. The tests with the new module also show consistency with GRASP tests that are traditionally configured for ground-based AERONET measurements.

We also tested the algorithm with real measurements. Application of the GRASP/Component algorithm to the AERONET Sun/sky photometric measurements retrievals of AOT, Ångström Exponent and SSA presented good agreement with the standard operational AERONET product for sites dominated by dust, biomass burning, and mixtures of dust and biomass burning aerosol. In addition, because of the reduced number of parameters (instead of 8 parameters for complex refractive index retrievals using 6 parameters for component retrievals) and an additional physical constraint on spectral dependence of refractive index in the component retrieval, the GRASP/Component approach applied for AERONET can split the characteristics of fine and coarse mode aerosol. The GRASP/Component algorithm was also applied for the POLDER/PARASOL satellite observations. An inter-comparison of aerosol optical characteristics derived from POLDER/PARASOL using the component approach and those of the AERONET operational product demonstrated a high reliability of the results.

The performance of the aerosol component algorithm has been demonstrated by the application to POLDER/PARASOL observations on the global scale for year 2008. The obtained spatial and temporal patterns of aerosol component distribution seem to agree well with known physical expectations. For a proper interpretation of the obtained results it should be also realized that the retrieved aerosol species and their concentrations compose a set of parameters that reproduces well the measured radiation field and provides adequate retrieved optical properties of aerosol. At the same time, the direct interpretation from the chemical point of view is not always evident and even possible. For instance, as mentioned in the methodology part, distinguishing some species is not possible for the given configuration of remote sensing measurements. However, the retrieved components still reflect the aerosol microphysics and chemistry, and their variability. One should also remember that, based on the sensitivity tests and experience of aerosol characterization by remote

sensing, the accuracy of the retrievals depends on the aerosol loading (AOT). Accuracy of the absorbing components retrieval can be primarily affected. Thus, interpretation of all the obtained patterns requires a more detailed analysis and we realize that some erroneous component features can be possible. The principal limitations of the presented approach are: (i) lack of sensitivity to absorption species in case of low AOT; (ii) difficulty to distinguish between iron oxide and absorbing carbonaceous species (BrC and BC), which is mainly related to the limited number of spectral channels in the shortwave solar spectrum; (iii) non-absorbing insoluble component can include organic material, but also non-absorbing dust. These assumptions can lead to some misinterpretation; for instance, the analysis of the BrC retrievals at some locations reveals that the aerosol absorbing properties attributed to BrC should be attributed to the iron oxides that are present in the fine size fraction. A post-retrieval classification is helpful to resolve the shortcomings. For example, analysis of Ångström Exponent can indicate dominance of coarse particles of mineral dust origin or fine particles of combustion origin, which can provide more information about the non-absorbing insoluble component.

Nevertheless, the results are encouraging. For example, the derived BC and BrC exhibit a seasonal and spatial variability that is attributed to the known biomass burning season cycle in Africa and the anthropogenic pollution patterns in Asia, in particular India and China. Coarse mode absorbing (mainly iron oxides) and non-absorbing (mainly dust) insoluble components show a similar seasonal and spatial variability, reaching a peak during MAM and a minimum during SON. It is also noted that the maximums of iron oxide concentration are not co-located with those of dust, because the elemental and mineralogical components of mineral dust vary depending on the source region. The global dust belt extending from western Africa, through the Middle East to Central Asia is also observed in the component retrieval. GRASP/Component indicates high concentrations of non-absorbing insoluble appear over the Sahara, Arabian Peninsula, Caspian Sea and Aral Sea regions in Central Asia, and the Gobi and Taklimakan desert in China. In addition, dust was also detected over some regions in Australia during DJF and SON.

The component retrieval algorithm demonstrated here using AERONET and POLDER/PARASOL data can also be used for interpreting other observations. That is, the component approach is now incorporated in the GRASP algorithm, which has a generalized input and can be easily modified and adapted to other both passive and active remote sensing instruments, for example, the Directional Polarimetric Camera (DPC) launched onboard the GaoFen-5 Satellite in Chinese High-resolution Earth Observation Program, which is the first Chinese multi-angle polarized earth observation satellite sensor (Dubovik et al., 2019; Li et al., 2018). Moreover, the proposed aerosol parameterization using components can be helpful not only for retrieving additional information about aerosol component, but also for optimizing retrieval stability.

Additionally, we tested the volume-weighted mixing model, in addition to the Maxwell-Garnett EMA, to evaluate the sensitivity of our approach to the assumed aerosol EMA. We tested both approaches using our suite of aerosol species (i.e. BC, BrC, coarse mode absorbing insoluble, fine and coarse mode non-absorbing insoluble). The sensitivity tests revealed that implementation of the volume-weighted mixing rule also presents stable results that are consistent with the Maxwell-Garnett EMA. Thus, the volume-weighted model can also be employed in GRASP/Component retrieval, and may be preferable in some applications due to its simplicity.

The results of the aerosol component retrieval from AERONET and POLDER/PARASOL satellite measurements demonstrate a potential for constraining global and regional aerosol modeling that can be particularly valuable because no other aerosol component data are often available on a large spatial and temporal scale.

Data availability: The retrievals can be requested directly from the corresponding author (oleg.dubovik@univ-lille.fr or yevgeny.derimian@univ-lille.fr)

Author contributions: LL, OD, YD and GLS developed the retrieval algorithm, designed and realized the sensitivity and uncertainty tests and applied the algorithm to the real data. OD with contributions of YD and GLS suggested the aerosol component retrieval conception. TL, PL, AL, FD, DF and CC contributed to the modifications of the GRASP code and application to the satellite data. BT and AL contributed in application to the AERONET data. ZL and HC supported the work and provided expertise on Asian aerosol observations. LL, YD and OD wrote the paper with input from all the authors.

Competing interests: The authors declare that they have no conflict of interest.

Acknowledgments

This work is supported by the Labex CaPPA (Laboratory of Excellence − Chemical and Physical Properties of the Atmosphere) project, which is funded by the French National Research Agency (ANR) through the PIA (Programme d'Investissement d'Avenir) under contract "ANR-11-LABX-0005-01". This work is also financially supported by the National Science Fund for Distinguished Young Scholars (grant no. 41825011), National Key R&D Program of China (2016YFA0601901). The authors thank CNES and ICARE data distribution center for POLDER/PARASOL data and the entire AERONET team, especially the principal investigators of the AERONET sites used in this study, for their long-term efforts to maintain AERONET observation. The authors acknowledge suggestions of Mian Chin (NASA GSFC) on connection and comparison with global chemical transport models and of Lorraine A. Remer (UMBC) about understanding of the results and the uncertainties.

1243

1244 **Reference**:

1245

1246 Abel, S.J., Haywood, J.M., Highwood, E.J., Li, J., Buseck, P.R.: Evolution of biomass
1247   burning aerosol properties from an agricultural fire in southern Africa, Geophys. Res.
1248   Lett., 30, 10–13, https://doi.org/10.1029/2003GL017342, 2003.
1249 Alfaro, S., Lafon, S., Rajot, J., Formenti, P., Gaudichet, A., and Maille, M.: Iron oxides and
1250   light absorption by pure desert dust: an experimental study, J. Geophys. Res., 109,
1251   D08208, doi:10.1029/2003JD004374, 2004.
1252 Alizadeh Choobari, O., Zawar-Reza, P., Sturman, A.: Low level jet intensification by mineral
1253   dust aerosols, Ann. Geophys., 31, 625–632, https://doi.org/10.5194/angeo-31-625-2013,
1254   2013.
1255 Andreae, M.O. and Gelencsér, A.: Black carbon or brown carbon? the nature of light-
1256   absorbing carbonaceous aerosols, Atmos. Chem. Phys., 6, 3131–3148,
1257   https://doi.org/10.5194/acp-6-3131-2006, 2006.
1258 Arimoto, R., Balsam, W., Schloesslin, C.: Visible spectroscopy of aerosol particles collected
1259   on filters: Iron-oxide minerals, Atmos. Environ., 36, 89–96,
1260   https://doi.org/10.1016/S1352-2310(01)00465-4, 2002.
1261 Arola, A., Schuster, G., Myhre, G., Kazadzis, S., Dey, S., Tripathi, S.N.: Inferring absorbing
1262   organic carbon content from AERONET data, Atmos. Chem. Phys., 11, 215–225,
1263   https://doi.org/10.5194/acp-11-215-2011, 2011.
1264 Bahadur, R., Praveen, P., Xu, Y., and Ramanathan, V.: Solar absorption by elemental and
1265   brown carbon determined from spectral observations, P. Natl. Acad. Sci. USA, 109,
1266   17366–17371, https://doi.org/10.1073/pnas.1205910109, 2012.
1267 Benavent-oltra, J.A., Román, R., Granados-muñoz, M.J., Pérez-ramírez, D.: Comparative
1268   assessment of GRASP algorithm for a dust event over Granada (Spain) during
1269   ChArMEx-ADRIMED 2013 campaign, Atmos. Meas. Tech., 10, 4439–4457,
1270   https://doi.org/10.5194/amt-10-4439-2017, 2017.
1271 Bitan, A. and Sa'Aroni, H.: The horizontal and vertical extension of the Persian Gulf pressure
1272   trough, Int. J. Climatol., 12, 733–747, https://doi.org/10.1002/joc.3370120706, 1992.
1273 Bohren, C.F. and Huffman, D.R.: Scattering Coefficients, in: Absorption and Scattering of
1274   Light by Small Particles, 1983.
1275 Bond, T.C. and Bergstrom, R.W.: Light Absorption by Carbonaceous Particles: An
1276   Investigative Review, Aerosol Sci. Technol., 40, 27–67,
1277   https://doi.org/10.1080/02786820500421521, 2006.
1278 Bond, T.C., Charlson, R.J., Heintzenberg, J.: Quantifying the emission of light-absorbing
1279   particles: Measurements tailored to climate studies, Geophys. Res. Lett., 25, 337–340,
1280   https://doi.org/10.1029/98GL00039, 1998.
1281 Bond, T.C., Doherty, S.J., Fahey, D.W., Forster, P.M., Berntsen, T., Deangelo, B.J., Flanner,
1282   M.G., Ghan, S., Kärcher, B., Koch, D., Kinne, S., Kondo, Y., Quinn, P.K., Sarofim,
1283   M.C., Schultz, M.G., Schulz, M., Venkataraman, C., Zhang, H., Zhang, S., Bellouin, N.,
1284   Guttikunda, S.K., Hopke, P.K., Jacobson, M.Z., Kaiser, J.W., Klimont, Z., Lohmann,
1285   U., Schwarz, J.P., Shindell, D., Storelvmo, T., Warren, S.G., Zender, C.S.: Bounding the
1286   role of black carbon in the climate system: A scientific assessment, J. Geophys. Res.
1287   Atmos., 118, 5380–5552, https://doi.org/10.1002/jgrd.50171, 2013.
1288 Brindley, H., Osipov, S., Bantges, R., Smirnov, A., Banks, J., Levy, R., Jish Prakash, P.,
1289   Stenchikov, G.: An assessment of the quality of aerosol retrievals over the Red Sea and
1290   evaluation of the climatological cloud-free dust direct radiative effect in the region, J.
1291   Geophys. Res. Atmos., 120, 10862-10878, https://doi.org/10.1002/2015JD023282,
1292   2015.
1293 Cahoon, D.R., Stocks, B.J., Levine, J.S., Cofer, W.R., O'Neill, K.P.: Seasonal distribution of
1294   African savanna fires, Nature, 359, 812–815, https://doi.org/10.1038/359812a0, 1992.
1295 Chakrabarty, R.K., Moosmüller, H., Chen, L.W.A., Lewis, K., Arnott, W.P., Mazzoleni, C.,
1296   Dubey, M.K., Wold, C.E., Hao, W.M., Kreidenweis, S.M.: Brown carbon in tar balls

from smoldering biomass combustion, Atmos. Chem. Phys., 10, 6363–6370, https://doi.org/10.5194/acp-10-6363-2010, 2010.

Chami, M., Santer, R., Dilligeard, E.: Radiative transfer model for the computation of radiance and polarization in an ocean–atmosphere system: polarization properties of suspended matter for remote sensing, Appl. Opt., 40, 2398, https://doi.org/10.1038/laban1011-313, 2001.

Chen, C., Dubovik, O., Henze, D.K., Lapyonak, T., Chin, M., Ducos, F., Litvinov, P., Huang, X., Li, L.: Retrieval of desert dust and carbonaceous aerosol emissions over Africa from POLDER/PARASOL products generated by the GRASP algorithm, Atmos. Chem. Phys., 18, 12551–12580, https://doi.org/10.5194/acp-18-12551-2018, 2018.

Chen, C., Dubovik, O., Henze, D. K., Chin, M., Lapyonak, T., Schuster, G. L., Ducos, F., Fuertes, D., Litvinov, P., Li, L., Lopatin, A., Hu, Q., and Torres, B.: Constraining global aerosol emissions using POLDER/PARASOL satellite remote sensing observations, Atmos. Chem. Phys. Discuss., https://doi.org/10.5194/acp-2019-623, in review, 2019.

Chen, C.T. and Cahan, B.D.: Visible and ultraviolet optical properties of single-crystal and polycrystalline hematite measured by spectroscopic ellipsometry, J. Opt. Soc. Am., 71, 932–934, 1981.

Chen, Y. and Bond, T.C.: Light absorption by organic carbon from wood combustion, Atmos. Chem. Phys., 10, 1773–1787, 2010.

Choobari, O.A., Zawar-Reza, P., Sturman, A.: The global distribution of mineral dust and its impacts on the climate system: A review, Atmos. Res., 138, 152–165, https://doi.org/10.1016/j.atmosres.2013.11.007, 2014.

Chowdhary, J., Cairns, B., Travis, L.D.: Contribution of water-leaving radiances to multiangle, multispectral polarimetric observations over the open ocean: bio-optical model results for case 1 waters, Appl. Opt., 45, 5542–67, https://doi.org/10.1364/AO.45.005542, 2006.

Chung, C., Ramanathan, V., and Decremer, D.: Observationally constrained estimates of carbonaceous aerosol radiative forcing, P. Natl. Acad. Sci. USA, 109, 11624–11629, https://doi.org/10.1073/pnas.1203707109, 2012.

Collins, W.D., Rasch, P.J., Eaton, B.E., Khattatov, B. V, Lamarque, J.-F., Zender, C.S.: Simulating aerosols using a chemical transport model with assimilation of satellite aerosol retrievals: Methodology for INDOEX, J. Geophys. Res. Atmos., 106, 7313–7336, https://doi.org/10.1029/2000JD900507, 2001.

Cooke, W.F., Liousse, C., Cachier, H., Feichter, J.: Construction of a $1° \times 1°$ fossil fuel emission data set for carbonaceous aerosol and implementation and radiative impact in the ECHAM4 model, J. Geophys. Res. Atmos., 104, 22137–22162, https://doi.org/10.1029/1999JD900187, 1999.

Cox, C. and Munk, W.: Measurement of the Roughness of the Sea Surface from Photographs of the Sun's Glitter, J. Opt. Soc. Am., 44, 838, https://doi.org/10.1364/JOSA.44.000838, 1954.

Craddock, R.A. and Greeley, R.: Minimum estimates of the amount and timing of gases released into the martian atmosphere from volcanic eruptions, Icarus, 204, 512–526, https://doi.org/10.1016/j.icarus.2009.07.026, 2009.

de Leeuw, G., Holzer-Popp, T., Bevan, S., Davies, W.H., Descloitres, J., Grainger, R.G., Griesfeller, J., Heckel, A., Kinne, S., Klüser, L., Kolmonen, P., Litvinov, P., Martynenko, D., North, P., Ovigneur, B., Pascal, N., Poulsen, C., Ramon, D., Schulz, M., Siddans, R., Sogacheva, L., Tanré, D., Thomas, G.E., Virtanen, T.H., von Hoyningen Huene, W., Vountas, M., Pinnock, S.: Evaluation of seven European aerosol optical depth retrieval algorithms for climate analysis, Remote Sens. Environ., 162, 295–315, https://doi.org/10.1016/j.rse.2013.04.023, 2015.

Decesari, S., Facchini, M.C., Carbone, C., Giulianelli, L., Rinaldi, M., Finessi, E., Fuzzi, S., Marinoni, A., Cristofanelli, P., Duchi, R., Bonasoni, P., Vuillermoz, E., Cozic, J., Jaffrezo, J.L., Laj, P.: Chemical composition of PM10 and PM1 at the high-altitude Himalayan station Nepal Climate Observatory-Pyramid (NCO-P) (5079 m a.s.l.), Atmos. Chem. Phys., 10, 4583–4596, https://doi.org/10.5194/acp-10-4583-2010, 2010.

1352 Derimian, Y., Choel, M., Rudich, Y., Deboudt, K., Dubovik, O., Laskin, A., Legrand, M.,
1353   Damiri, B., Koren, I., Unga, F., Moreau, M., Andreae, M. O., Karnieli, A.: Effect of sea
1354   breeze circulation on aerosol mixing state and radiative properties in a desert setting,
1355   Atmos. Chem. Phys., 17, 11331-11353, https://doi.org/10.5194/acp-17-11331-2017,
1356   2017.
1357 Derimian, Y., Karnieli, A., Kaufman, Y.J., Andreae, M.O., Andreae, T.W., Dubovik, O.,
1358   Maenhaut, W., Koren, I.: The role of iron and black carbon in aerosol light absorption,
1359   Atmos. Chem. Phys., 8, 3632–3637, 2008.
1360 Deschamps, P.Y., Buriez, J.C., Bréon, F.M., Leroy, M., Podaire, A., Bricaud, A., Sèze, G. :
1361   The POLDER Mission: Instrument Characteristics and Scientific Objectives, IEEE
1362   Trans. Geosci. Remote Sens., 32, 598–615, https://doi.org/10.1109/36.297978, 1994.
1363 Deuzé, J.L., Bréon, F.M., Devaux, C., Goloub, P., Herman, M., Lafrance, B., Maignan, F.,
1364   Marchand, A., Nadal, F., Perry, G., Tanré, D.: Remote sensing of aerosols over land
1365   surfaces from POLDER-ADEOS-1 polarized measurements, J. Geophys. Res. Atmos.,
1366   106, 4913–4926, https://doi.org/10.1029/2000JD900364, 2001.
1367 Dinar, E., Abo Riziq, A., Spindler, C., Erlick, C., Kiss, G., Rudich, Y., The complex
1368   refractive index of atmospheric and model humic-like substances (HULIS) retrieved by
1369   a cavity ring down aerosol spectrometer (CRD-AS), Faraday Discuss., 137, 279–295,
1370   https://doi.org/10.1039/b703111d, 2007.
1371 Downing, H.D. and Williams, D.: Optical constants of water in the infrared, J. Geophys. Res.,
1372   80, 1656–1661, https://doi.org/10.1029/JC080i012p01656, 1975.
1373 Dubovik, O.: Optimization of Numerical Inversion in Photopolarimetric Remote Sensing, in:
1374   Photopolarimetry in Remote Sensing, Kluwer Academic Publishers, Dordrecht, pp. 65–
1375   106, https://doi.org/10.1007/1-4020-2368-5_3, 2004.
1376 Dubovik, O., Herman, M., Holdak, A., Lapyonok, T., Tanré, D., Deuzé, J.L., Ducos, F.,
1377   Sinyuk, A., Lopatin, A.: Statistically optimized inversion algorithm for enhanced
1378   retrieval of aerosol properties from spectral multi-angle polarimetric satellite
1379   observations, Atmos. Meas. Tech., 4, 975–1018, https://doi.org/10.5194/amt-4-975-
1380   2011, 2011.
1381 Dubovik, O., Holben, B., Eck, T.F., Smirnov, A., Kaufman, Y.J., King, M.D., Tanré, D.,
1382   Slutsker, I.: Variability of Absorption and Optical Properties of Key Aerosol Types
1383   Observed in Worldwide Locations, J. Atmos. Sci., 59, 590–608, 2002a.
1384 Dubovik, O., Holben, B.N., Lapyonok, T., Sinyuk, A., Mishchenko, M.I., Yang, P., Slutsker,
1385   I.: Non-spherical aerosol retrieval method employing light scattering by spheroids,
1386   Geophys. Res. Lett., 29, 541-544, https://doi.org/10.1029/2001GL014506, 2002b.
1387 Dubovik, O. and King, M.D.: A flexible inversion algorithm for retrieval of aerosol optical
1388   properties from Sun and sky radiance measurements, J. Geophys. Res. Atmos., 105,
1389   20673–20696, https://doi.org/10.1029/2000JD900282, 2000.
1390 Dubovik, O., Lapyonok, T., Kaufman, Y.J., Chin, M., Ginoux, P., Kahn, R.A., Sinyuk, A.:
1391   Retrieving global aerosol sources from satellites using inverse modeling, Atmos. Chem.
1392   Phys., 8, 209–250, https://doi.org/10.5194/acp-8-209-2008, 2008.
1393 Dubovik, O., Lapyonok, T., Litvinov, P., Herman, M., Fuertes, D., Ducos, F., Torres, B.,
1394   Derimian, Y., Huang, X., Lopatin, A., Chaikovsky, A., Aspetsberger, M., Federspiel, C.:
1395   GRASP: a versatile algorithm for characterizing the atmosphere, SPIE Newsroom 2–5,
1396   https://doi.org/10.1117/2.1201408.005558, 2014.
1397 Dubovik, O., Li, Z., Mishchenko, M.I., Tanré, D., Karol, Y., Bojkov, B., Cairns, B., Diner,
1398   D.J., Espinosa, W.R., Goloub, P., Gu, X., Hasekamp, O., Hong, J., Hou, W.,
1399   Knobelspiesse, K.D., Landgraf, J., Li, L., Litvinov, P., Liu, Y., Lopatin, A., Marbach,
1400   T., Maring, H., Martins, V., Meijer, Y., Milinevsky, G., Mukai, S., Parol, F., Qiao, Y.,
1401   Remer, L., Rietjens, J., Sano, I., Stammes, P., Stamnes, S., Sun, X., Tabary, P., Travis,
1402   L.D., Waquet, F., Xu, F., Yan, C., Yin, D.: Polarimetric remote sensing of atmospheric
1403   aerosols: Instruments, methodologies, results, and perspectives, J. Quant. Spectrosc.
1404   Radiat. Transf., 224, 474–511, https://doi.org/10.1016/j.jqsrt.2018.11.024, 2019.
1405 Dubovik, O., Sinyuk, A., Lapyonok, T., Holben, B.N., Mishchenko, M., Yang, P., Eck, T.F.,
1406   Volten, H., Muñoz, O., Veihelmann, B., van der Zande, W.J., Leon, J.F., Sorokin, M.,

Slutsker, I.: Application of spheroid models to account for aerosol particle nonsphericity in remote sensing of desert dust, J. Geophys. Res. Atmos., 111, 1–34, https://doi.org/10.1029/2005JD006619, 2006.

Duncan, B.N., Martin, R. V., Staudt, A.C., Yevich, R., Logan, J.A.: Interannual and seasonal variability of biomass burning emissions constrained by satellite observations, J. Geophys. Res., 108, 4100, https://doi.org/10.1029/2002JD002378, 2003.

Edmonds, M., Sides, I.R., Swanson, D.A., Werner, C., Martin, R.S., Mather, T.A., Herd, R.A., Jones, R.L., Mead, M.I., Sawyer, G., Roberts, T.J., Sutton, A.J., Elias, T.: Magma storage, transport and degassing during the 2008-10 summit eruption at Kilauea Volcano, Hawaii, Geochim. Cosmochim. Acta., 123, 284–301, https://doi.org/10.1016/j.gca.2013.05.038, 2013.

Espinosa, W.R., Remer, L.A., Dubovik, O., Ziemba, L., Beyersdorf, A., Orozco, D., Schuster, G., Lapyonok, T., Fuertes, D., Martins, J.V.: Retrievals of aerosol optical and microphysical properties from Imaging Polar Nephelometer scattering measurements, Atmos. Meas. Tech., 10, 811–824, https://doi.org/10.5194/amt-10-811-2017, 2017.

Falkovich, A. H., Schkolnik, G., Ganor, E., Rudich, Y.: Adsorption of organic compounds pertinent to urban environments onto mineral dust particles, J. Geophys. Res. Atmos., 109, https://doi.org/10.1029/2003jd003919, 2004.

Formenti, P., Caquineau, S., Chevaillier, S., Klaver, A., Desboeufs, K., Rajot, J.L., Belin, S., Briois, V.: Dominance of goethite over hematite in iron oxides of mineral dust from Western Africa: Quantitative partitioning by X-ray absorption spectroscopy, J. Geophys. Res. Atmos., 119, 12740-12754, https://doi.org/10.1002/2014JD021668, 2014.

Formenti, P., Rajot, J.L., Desboeufs, K., Caquineau, S., Chevaillier, S., Nava, S., Gaudichet, A., Journet, E., Triquet, S., Alfaro, S., Chiari, M., Haywood, J., Coe, H., Highwood, E.: Regional variability of the composition of mineral dust from western Africa: Results from the AMMA SOP0/DABEX and DODO field campaigns, J. Geophys. Res. Atmos., 113, 1–12, https://doi.org/10.1029/2008JD009903, 2008.

Ganor, E. and Foner, H. A.: The mineralogical and chemical properties and the behavior of aeolian Saharan dust over Israel, in: The Impact of Desert Dust Across the Mediterranean, edited by: Guerzoni, S., and Chester, R., Kluwer Academic Publishers, Printed in the Netherlands, 163-172, 1996.

Ganor, E., Foner, H.A., Bingemer, H.G., Udisti, R., Setter, I.: Biogenic sulphate generation in the Mediterranean Sea and its contribution to the sulphate anomaly in the aerosol over Israel and the Eastern Mediterranean, Atmos. Environ., 34, 3453–3462, https://doi.org/10.1016/S1352-2310(00)00077-7, 2000.

Gasse, F.: Diatom-inferred salinity and carbonate oxygen isotopes in Holocene waterbodies of the western Sahara and Sahel (Africa), Quat. Sci. Rev., 21, 737–767, https://doi.org/10.1016/S0277-3791(01)00125-1, 2002.

Ghosh, G.: Dispersion-equation coefficients for the refractive index and birefringence of calcite and quartz crystals, Opt. Commun., 163, 95–102, https://doi.org/10.1016/S0030-4018(99)00091-7, 1999.

Ginoux, P., Prospero, J.M., Gill, T.E., Hsu, N.C., Zhao, M.: Global-scale attribution of anthropogenic and natural dust sources and their emission rates based on MODIS Deep Blue aerosol products, Rev. Geophys., 50, 1–36, https://doi.org/10.1029/2012RG000388, 2012.

Gosse, S.F., Wang, M., Labrie, D., Chylek, P.: Imaginary part of the refractive index of sulfates and nitrates in the 0.7-2.6-micron spectral region, Appl. Opt., 36, 3622–3634, 1997.

Goudie, A.S.: Desert dust and human health disorders, Environ. Int., 63, 101–113, https://doi.org/10.1016/j.envint.2013.10.011, 2014.

Guieu, C., Loye-Pilot, M. D., Ridame, C., Thomas, C.: Chemical characterization of the Saharan dust end-member: Some biogeochemical implications for the western Mediterranean Sea, J. Geophys. Res., 107 (D15), 4258, https://doi.org/4210.1029/2001JD000582, 2002.

Hammer, M.S., Martin, R.V., Li, C., Torres, O., Manning, M., Boys, B.L.: Insight into global

trends in aerosol composition from 2005 to 2015 inferred from the OMI Ultraviolet Aerosol Index, Atmos. Chem. Phys., 18, 8097–8112, https://doi.org/10.5194/acp-18-8097-2018, 2018.

Hale, G.M. and Querry, M.R.: Optical Constants of Water in the 200-nm to 200-microm Wavelength Region, Appl. Opt., 12, 555–563, https://doi.org/10.1364/AO.12.000555, 1973.

Haywood, J.M., Osborne, S.R., Francis, P.N., Keil, A., Formenti, P., Andreae, M.O., Kaye, P.H.: The mean physical and optical properties of regional haze dominated by biomass burning aerosol measured from the C-130 aircraft during SAFARI 2000, J. Geophys. Res. Atmos., 108, 1–9, https://doi.org/10.1029/2002JD002226, 2003.

Haywood, J. M., Pelon, J., Formenti, P., Bharmal, N., Brooks, M., Capes, G., Chazette, P., Chou, C., Christopher, S., Coe, H., Cuesta, J., Derimian, Y., Desboeufs, K., Greed, G., Harrison, M., Heese, B., Highwood, E. J., Johnson, B., Mallet, M., Marticorena, B., Marsham, J., Milton, S., Myhre, G., Osborne, S. R., Parker, D. J., Rajot, J. L., Schulz, M., Slingo, A., Tanre, D., Tulet, P.: Overview of the Dust and Biomass-burning Experiment and African Monsoon Multidisciplinary Analysis Special Observing Period-0, J. Geophys. Res. Atmos., 113, https://doi.org/10.1029/2008jd010077, 2008.

Haywood, J.M. and Shine, K.P.: The effect of anthropogenic sulfate and soot aerosol on the clear sky planetary radiation budget, Geophys. Res. Lett., 22, 603–606, https://doi.org/10.1029/95GL00075, 1995.

Henze, D.K., Hakami, A., Seinfeld, J.H.: Development of the adjoint of GEOS-Chem, Atmos. Chem. Phys., 7, 2413–2433, https://doi.org/10.5194/acp-7-2413-2007, 2007.

Herman, M., Deuzé, J.L., Marchand, A., Roger, B., Lallart, P.: Aerosol remote sensing from POLDER/ADEOS over the ocean: Improved retrieval using a nonspherical particle model, J. Geophys. Res. D Atmos., 110, 1–11, https://doi.org/10.1029/2004JD004798, 2005.

Herrmann, L., Stahr, K., Jahn, R.: The importance of source region identification and their properties for soil-derived dust: The case of Harmattan dust sources for eastern West Africa, Contrib. to Atmos. Phys., 72, 141–150, 1999.

Hoffer, A., Gelencsér, A., Guyon, P., Kiss, G., Schmid, O., Frank, G.P., Artaxo, P., Andreae, M.O.: Optical properties of humic-like substances (HULIS) in biomass-burning aerosols, Atmos. Chem. Phys., 6, 3563–3570, https://doi.org/10.5194/acp-6-3563-2006, 2006.

Jacobson, M.Z.: Isolating nitrated and aromatic aerosols and nitrated aromatic gases as sources of ultraviolet light absorption, J. Geophys. Res. Atmos., 104, 3527–3542, https://doi.org/10.1029/1998JD100054, 1999.

Jickells, T.D., An, Z.S., Andersen, K.K., Baker, A.R., Bergametti, C., Brooks, N., Cao, J.J., Boyd, P.W., Duce, R.A., Hunter, K.A., Kawahata, H., Kubilay, N., LaRoche, J., Liss, P.S., Mahowald, N., Prospero, J.M., Ridgwell, A.J., Tegen, I., Torres, R.: Global iron connections between desert dust, ocean biogeochemistry, and climate, Science, 308, 67–71, https://doi.org/10.1126/science.1105959, 2005.

Journet, E., Balkanski, Y., Harrison, S.P.: A new data set of soil mineralogy for dust-cycle modeling, Atmos. Chem. Phys., 14, 3801–3816, https://doi.org/10.5194/acp-14-3801-2014, 2014.

Kahn, R.A. and Gaitley, B.J.: An analysis of global aerosol type as retrieved by MISR, J. Geophys. Res. Atmos., 120, 4248–4281, https://doi.org/10.1002/2015JD023322, 2015.

Kanakidou, M., Seinfeld, J.H., Pandis, S.N., Barnes, I., Dentener, F.J., Facchini, M.C., Van Dingenen, R., Ervens, B., Nenes, A., Nielsen, C.J., Swietlicki, E., Putaud, J.P., Balkanski, Y., Fuzzi, S., Horth, J., Moortgat, G.K., Winterhalter, R., Myhre, C.E.L., Tsigaridis, K., Vignati, E., Stephanou, E.G., Wilson, J.: Organic aerosol and global climate modelling: a review, Atmos. Chem. Phys., 5, 1053–1123, https://doi.org/10.5194/acp-5-1053-2005, 2005.

Kerker, M., Scheiner, P., Cooke, D.D., Kratohvil, J.P.: Absorption index and color of colloidal hematite, J. Colloid Interface Sci., 71, 176–187, https://doi.org/10.1016/0021-9797(79)90231-5, 1979.

Kirchstetter, T.W., Novakov, T., Hobbs, P. V.: Evidence that the spectral dependence of light absorption by aerosols is affected by organic carbon, J. Geophys. Res. Atmos., 109. https://doi.org/10.1029/2004JD004999, 2004.

Koepke, P.: Effective reflectance of oceanic whitecaps, Appl. Opt., 23, 1816, https://doi.org/10.1364/AO.23.001816, 1984.

Koepke, P., Hess, M., Schult, I., Shettle, E.P.: Global Aerosol Data Set, Max-Planck-Institut fur Meteorologie, https://doi.org/ISSN: 0937-1060, 1997.

Koren, I., Kaufman, Y.J.: Direct wind measurements of Saharan dust events from Terra and Aqua satellites, Geophys. Res. Lett., 31, 1–4, https://doi.org/10.1029/2003GL019338, 2004.

Kou, L., Labrie, D., Chylek, P.: Refractive indices of water and ice in the 0.65 to 2.5 μm spectral range, Appl. Opt., 32, 3531, https://doi.org/10.1364/AO.32.003531, 1993.

Koven, C.D. and Fung, I.: Inferring dust composition from wavelength-dependent absorption in Aerosol Robotic Network (AERONET) data, J. Geophys. Res. Atmos., 111, https://doi.org/10.1029/2005JD006678, 2006.

Krueger, B.J., Grassian, V.H., Cowin, J.P., Laskin, A.: Heterogeneous chemistry of individual mineral dust particles from different dust source regions: The importance of particle mineralogy, Atmos. Environ., 38, 6253–6261, https://doi.org/10.1016/j.atmosenv.2004.07.010, 2004.

Lafon, S., Rajot, J. L., Alfaro, S. C., Gaudichet, A.: Quantification of iron oxides in desert aerosol, Atmos. Environ., 38, 1211-1218, 2004.

Lafon, S., Sokolik, I.N., Rajot, J.L., Caquincau, S., Gaudichet, A.: Characterization of iron oxides in mineral dust aerosols: Implications for light absorption, J. Geophys. Res. Atmos., 111, 1–19, https://doi.org/10.1029/2005JD007016, 2006.

Laskin, A., Iedema, M. J., Ichkovich, A., Graber, E. R., Taraniuk, I., Rudich, Y.: Direct observation of completely processed calcium carbonate dust particles, Faraday Discuss., 130, 453-468, https://doi.org/10.1039/b417366j, 2005.

Lázaro, F.J., Gutiérrez, L., Barrón, V., Gelado, M.D.: The speciation of iron in desert dust collected in Gran Canaria (Canary Islands): Combined chemical, magnetic and optical analysis, Atmos. Environ., 42, 8987–8996, https://doi.org/10.1016/j.atmosenv.2008.09.035, 2008.

Lelieveld, J., Berresheim, H., Borrmann, S., Crutzen, P.J., Dentener, F.J., Fischer, H., Feichter, J., Flatau, P.J., Heland, J., Holzinger, R., Korrmann, R., Lawrence, M.G., Levin, Z., Markowicz, K.M., Mihalopoulos, N., Minikin, A., Ramanathan, V., De Reus, M., Roelofs, G.J., Scheeren, H.A., Sciare, J., Schlager, H., Schultz, M., Siegmund, P., Steil, B., Stephanou, E.G., Stier, P., Traub, M., Warneke, C., Williams, J., Ziereis, H.: Global air pollution crossroads over the Mediterranean, Science, 298, 794–799, https://doi.org/10.1126/science.1075457, 2002.

Léon, J.F. and Legrand, M.: Mineral dust sources in the surroundings of the North Indian Ocean, Geophys. Res. Lett., 30, https://doi.org/10.1029/2002GL016690, 2003.

Lesins, G., Chylek, P., Lohmann, U.: A study of internal and external mixing scenarios and its effect on aerosol optical properties and direct radiative forcing, J. Geophys. Res. Atmos., 107, https://doi.org/10.1029/2001JD000973, 2002.

Levin, Z.: On the interactions of mineral dust, sea-salt particles, and clouds: A measurement and modeling study from the Mediterranean Israeli Dust Experiment campaign, J. Geophys. Res., 110, D20202, https://doi.org/10.1029/2005JD005810, 2005.

Levin, Z., Ganor, E., Gladstein, V.: The effects of desert particles coated with sulfate on rain formation in the Eastern Mediterranean, J. Appl. Meteorol., 35, 1511–1523, 1996.

Li, J., Pósfai, M., Hobbs, P. V., Buseck, P.R.: Individual aerosol particles from biomass burning in southern Africa: 2, Compositions and aging of inorganic particles, J. Geophys. Res. Atmos., 108, https://doi.org/10.1029/2002JD002310, 2003.

Li, X. and Strahler, A.H.: Geometric-Optical Bidirectional Reflectance Modeling of the Discrete Crown Vegetation Canopy: Effect of Crown Shape and Mutual Shadowing, IEEE Trans. Geosci. Remote Sens., 30, 276–292, https://doi.org/10.1109/36.134078, 1992.

Li, Z., Gu, X., Wang, L., Li, D., Xie, Y., Li, K., Dubovik, O., Schuster, G., Goloub, P., Zhang, Y., Li, L., Ma, Y., Xu, H.: Aerosol physical and chemical properties retrieved from ground-based remote sensing measurements during heavy haze days in Beijing winter, Atmos. Chem. Phys., 13, 10171–10183, https://doi.org/10.5194/acp-13-10171-2013, 2013.

Li, Z., Hou, W., Hong, J., Zheng, F., Luo, D., Wang, J., Gu, X., Qiao, Y.: Directional Polarimetric Camera (DPC): Monitoring aerosol spectral optical properties over land from satellite observation, J. Quant. Spectrosc. Radiat. Transf., 218, 21–37, https://doi.org/10.1016/j.jqsrt.2018.07.003, 2018.

Li, Z., Li, L., Zhang, F., Li, D., Xie, Y., Xu, H.: Comparison of aerosol properties over Beijing and Kanpur: Optical, physical properties and aerosol component composition retrieved from 12 years ground-based Sun-sky radiometer remote sensing data, J. Geophys. Res. Atmos., 120, 1520–1535, https://doi.org/10.1002/2014JD022593, 2015.

Liousse, C., Penner, J.E., Chuang, C., Walton, J.J., Eddleman, H., Cachier, H.: A global three-dimensional model study of carbonaceous aerosols, J. Geophys. Res., 101, 19411–19432, https://doi.org/10.1029/95JD03426, 1996.

Liu, H., Pinker, R.T., Holben, B.N.: A global view of aerosols from merged transport models, satellite, and ground observations, J. Geophys. Res. Atmos., 110, 1–16, https://doi.org/10.1029/2004JD004695, 2005.

Longtin, D.R., Shettle, E.P., Hummel, J.R., Pryce, J.D.: A Wind Dependent Desert Aerosol Dust Model: Radiative Properties, Scientific Report No.6, 1988.

Lopatin, A., Dubovik, O., Chaikovsky, A., Goloub, P., Lapyonok, T., Tanré, D., Litvinov, P.: Enhancement of aerosol characterization using synergy of lidar and Sun- photometer coincident observations : the GARRLiC algorithm, Atmos. Meas. Tech., 6, 2065–2088, https://doi.org/10.5194/amt-6-2065-2013, 2013.

Maenhaut, W., Salma, I., Cafmeyer, J., Annegarn, H.J., Andreae, M.O.: Regional atmospheric aerosol composition and sources in the eastern Transvaal, South Africa, and impact of biomass burning, J. Geophys. Res., 101, 23631, https://doi.org/10.1029/95JD02930, 1996.

Mahowald, N.M., Baker, A.R., Bergametti, G., Brooks, N., Duce, R.A., Jickells, T.D., Kubilay, N., Prospero, J.M., Tegen, I.: Atmospheric global dust cycle and iron inputs to the ocean. Global Biogeochem, Cycles, 19, https://doi.org/10.1029/2004GB002402, 2005.

Maignan, F., Bréon, F.M., Fédèle, E., Bouvier, M.: Polarized reflectances of natural surfaces: Spaceborne measurements and analytical modeling, Remote Sens. Environ., 113, 2642–2650, https://doi.org/10.1016/j.rse.2009.07.022, 2009.

Martonchik, J., Diner, D., Kahn, R., Verstraete, M., Pinty, B., Gordon, H., Ackerman, T.: Techniques for the retrieval of aerosol properties over land and ocean using multiangle data, IEEE Transactions on Geoscience and Remote Sensing, 36, 1212-1227, 1998.

Middleton, N.J.: A geography of dust storms in South-West Asia, J. Climatol., 6, 183–196, https://doi.org/10.1002/joc.3370060207, 1986a.

Middleton, N.J.: Dust storms in the Middle East, J. Arid Environ., 10, 83–96, https://doi.org/10.1016/S0140-1963(18)31249-7, 1986b.

Miri, A., Ahmadi, H., Ghanbari, A., Moghaddamnia, A.: Dust Storms Impacts on Air Pollution and Public Health under Hot and Dry Climate, Int. J. Energy Environ., 2, 101–105, 2007.

Miyazaki, Y., Kondo, Y., Takegawa, N., Komazaki, Y., Fukuda, M., Kawamura, K., Mochida, M., Okuzawa, K., Weber, R.J.: Time-resolved measurements of water-soluble organic carbon in Tokyo, J. Geophys. Res. Atmos., 111, 1–12, https://doi.org/10.1029/2006JD007125, 2006.

Orr, C., Hurd, F.K., Corbett, W.J.: Aerosol size and relative humidity, J. Colloid Sci., 13, 472–482, https://doi.org/10.1016/0095-8522(58)90055-2, 1958.

Ota, Y., Higurashi, A., Nakajima, T., Yokota, T.: Matrix formulations of radiative transfer including the polarization effect in a coupled atmosphere-ocean system, J. Quant. Spectrosc. Radiat. Transf., 111, 878–894, https://doi.org/10.1016/j.jqsrt.2009.11.021,

1627   2010.

1628 Palmer, K.F. and Williams, D.: Optical properties of water in the near infrared, J. Opt. Soc.
1629   Am., 64, 1107, https://doi.org/10.1364/JOSA.64.001107, 1974.

1630 Popp, T., De Leeuw, G., Bingen, C., Brühl, C., Capelle, V., Chedin, A., Clarisse, L.,
1631   Dubovik, O., Grainger, R., Griesfeller, J., Heckel, A., Kinne, S., Klüser, L., Kosmale,
1632   M., Kolmonen, P., Lelli, L., Litvinov, P., Mei, L., North, P., Pinnock, S., Povey, A.,
1633   Robert, C., Schulz, M., Sogacheva, L., Stebel, K., Zweers, D.S., Thomas, G., Tilstra,
1634   L.G., Vandenbussche, S., Veefkind, P., Vountas, M., Xue, Y.: Development, production
1635   and evaluation of aerosol climate data records from European satellite observations
1636   (Aerosol_cci), Remote Sens., 8, https://doi.org/10.3390/rs8050421, 2016.

1637 Pósfai, M., Simonics, R., Li, J., Hobbs, P. V., Buseck, P.R.: Individual aerosol particles from
1638   biomass burning in southern Africa1: Compositions and size distributions of
1639   carbonaceous particles, J. Geophys. Res. Atmos., 108,
1640   https://doi.org/10.1029/2002JD002291, 2003.

1641 Prospero, J.M., Ginoux, P., Torres, O., Nicholson, S.E., Gill, T.E.: Environmental
1642   characterization of global sources of atmospheric soil dust identified with the Nimbus 7
1643   Total Ozone Mapping Spectrometer (TOMS) absorbing aerosol product, Rev. Geophys.,
1644   40, 1–31, https://doi.org/10.1029/2000RG000095, 2002.

1645 Rashki, A., Rautenbach, C.J. d. W., Eriksson, P.G., Kaskaoutis, D.G., Gupta, P.: Temporal
1646   changes of particulate concentration in the ambient air over the city of Zahedan, Iran,
1647   Air Qual. Atmos. Heal., 6, 123–135, https://doi.org/10.1007/s11869-011-0152-5, 2013.

1648 Reid, J.S., Hobbs, P. V., Ferek, R.J., Blake, D.R., Martins, J.V., Dunlap, M.R., Liousse, C.:
1649   Physical, chemical, and optical properties of regional hazes dominated by smoke in
1650   Brazil, J. Geophys. Res. Atmos., 103, 32059–32080,
1651   https://doi.org/10.1029/98JD00458, 1998.

1652 Remer, L., Kaufman, Y., Tanré, D., Mattoo, S., Chu, D., Martins, J., Li, R., Ichoku, C., Levy,
1653   R., Kleidman, R., Eck, T., Vermote, E., and Holben, B.: The MODIS aerosol algorithm,
1654   products and validation, Journal of the Atmospheric Sciences, 62, 947-973, 2005.

1655 Román, R., Benavent-oltra, J.A., Casquero-vera, J.A., Lopatin, A., Cazorla, A., Lyamani, H.,
1656   Denjean, C., Fuertes, D., Perez-Ramirez, D., Torres, B., Toledano, C., Dubovik, O.,
1657   Cachorro, V.E., de Frutos, A.M., Olmo, F.J., Alados-Arboledas, L.: Retrieval of aerosol
1658   profiles combining sunphotometer and ceilometer measurements in GRASP code,
1659   Atmos. Res., 204, 161–177, https://doi.org/10.1016/j.atmosres.2018.01.021, 2018.

1660 Román, R., Torres, B., Fuertes, D., Cachorro, V.E., Dubovik, O., Toledano, C., Cazorla, A.,
1661   Barreto, A., Frutos, A. De, Alados-arboledas, L.: Remote sensing of lunar aureole with a
1662   sky camera : Adding information in the nocturnal retrieval of aerosol properties with
1663   GRASP code, Remote Sens. Environ., 196, 238–252,
1664   https://doi.org/10.1016/j.rse.2017.05.013, 2017.

1665 Roujean, J.-L., Leroy, M., Deschamps, P.-Y. : A bidirectional reflectance model of the
1666   Earth's surface for the correction of remote sensing data, J. Geophys. Res., 97, 20455,
1667   https://doi.org/10.1029/92JD01411, 1992.

1668 Russell, P., Kacenelenbogen, M., Livingston, J., Hasekamp, O., Burton, S., Schuster, G.,
1669   Johnson, M., Knobelspiesse, K., Redemann, J., Ramachandran, S., and Holben, B.: A
1670   multiparameter aerosol classification method and its application to retrievals from
1671   spaceborne polarimetry, J. Geophys. Res., 119, https://doi.org/10.1002/2013JD021411,
1672   2014.

1673 Schkolnik, G., Chand, D., Hoffer, A., Andreae, M.O., Erlick, C., Swietlicki, E., Rudich, Y.:
1674   Constraining the density and complex refractive index of elemental and organic carbon
1675   in biomass burning aerosol using optical and chemical measurements, Atmos. Environ.,
1676   41, 1107–1118, https://doi.org/10.1016/j.atmosenv.2006.09.035, 2007.

1677 Schmeisser, L., Andrews, E., Ogren, J. A., Sheridan, P., Jefferson, A., Sharma, S., Kim, J. E.,
1678   Sherman, J. P., Sorribas, M., Kalapov, I., Arsov, T., Angelov, C., Mayol-Bracero, O. L.,
1679   Labuschagne, C., Kim, S.-W., Hoffer, A., Lin, N.-H., Chia, H.-P., Bergin, M., Sun, J.,
1680   Liu, P., Wu, H.: Classifying aerosol type using in situ surface spectral aerosol optical
1681   properties, Atmos. Chem. Phys., 17, 12097–12120, https://doi.org/10.5194/acp-17-

1682   12097-2017, 2017.

1683   Schnaiter, M., Gimmler, M., Llamas, I., Linke, C., Jäger, C., Mutschke, H.: Strong spectral
1684   dependence of light absorption by organic carbon particles formed by propane
1685   combustion, Atmos. Chem. Phys., 6, 2981–2990, https://doi.org/10.5194/acp-6-2981-
1686   2006, 2006.

1687   Schuster, G.L., Dubovik, O., Arola, A.: Remote sensing of soot carbon – Part 1:
1688   Distinguishing different absorbing aerosol species, Atmos. Chem. Phys., 16, 1565–
1689   1585, https://doi.org/10.5194/acp-16-1565-2016, 2016a.

1690   Schuster, G.L., Dubovik, O., Arola, A., Eck, T.F., Holben, B.N.: Remote sensing of soot
1691   carbon – Part 2: Understanding the absorption Ångström exponent, Atmos. Chem.
1692   Phys., 16, 1587–1602, https://doi.org/10.5194/acp-16-1587-2016, 2016b.

1693   Schuster, G.L., Dubovik, O., Holben, B.N., Clothiaux, E.E.: Inferring black carbon content
1694   and specific absorption from Aerosol Robotic Network (AERONET) aerosol retrievals,
1695   J. Geophys. Res., 110, D10S17, https://doi.org/10.1029/2004JD004548, 2005.

1696   Schuster, G.L., Lin, B., Dubovik, O.: Remote sensing of aerosol water uptake, Geophys. Res.
1697   Lett., 36, https://doi.org/10.1029/2008GL036576, 2009.

1698   Shi, Z., Krom, M.D., Jickells, T.D., Bonneville, S., Carslaw, K.S., Mihalopoulos, N., Baker,
1699   A.R., Benning, L.G.: Impacts on iron solubility in the mineral dust by processes in the
1700   source region and the atmosphere: A review, Aeolian Res., 5, 21–42,
1701   https://doi.org/10.1016/j.aeolia.2012.03.001, 2012.

1702   Sokolik, I.N. and Toon, O.B.: Incorporation of mineralogical composition into models of the
1703   radiative properties of mineral aerosol from UV to IR wavelengths, J. Geophys. Res.
1704   Atmos., 104, 9423–9444, https://doi.org/10.1029/1998JD200048, 1999.

1705   Stone, E., Schauer, J., Quraishi, T.A., Mahmood, A. : Chemical characterization and source
1706   apportionment of fine and coarse particulate matter in Lahore, Pakistan, Atmos.
1707   Environ., 44, 1062–1070, https://doi.org/10.1016/j.atmosenv.2009.12.015, 2010.

1708   Streets, D.G., Gupta, S., Waldhoff, S.T., Wang, M.Q., Bond, T.C., Yiyun, B.: Black carbon
1709   emissions in China, Atmos. Environ., 35, 4281–4296, https://doi.org/10.1016/S1352-
1710   2310(01)00179-0, 2001.

1711   Sun, H., Biedermann, L., Bond, T.C.: Color of brown carbon: A model for ultraviolet and
1712   visible light absorption by organic carbon aerosol, Geophys. Res. Lett., 34,
1713   https://doi.org/10.1029/2007GL029797, 2007.

1714   Swap, R., Garstang, M., Macko, S.A., Tyson, P.D., Maenhaut, W., Artaxo, P., Kållberg, P.,
1715   Talbot, R.: The long-range transport of southern African aerosols to the tropical South
1716   Atlantic,   J.   Geophys.   Res.   Atmos.,   101,   23777–23791,
1717   https://doi.org/10.1029/95JD01049, 1996.

1718   Tang, I.N.: Chemical and size effects of hygroscopic aerosols on light scattering coefficients,
1719   J. Geophys. Res. Atmos., 101, 19245–19250, https://doi.org/10.1029/96JD03003, 1996.

1720   Tang, I.N.: Phase transformation and growth of aerosol particles composed of mixed salts, J.
1721   Aerosol Sci., 7361–7371, https://doi.org/10.1016/0021-8502(76)90022-7, 1976.

1722   Tang, I.N. and Munkelwitz, H.R.: Water activities, densities, and refractive indices of
1723   aqueous sulfates and sodium nitrate droplets of atmospheric importance 99, 18801–
1724   18808, 1994.

1725   Tang, I.N. and Munkelwitz, H.R.: Composition and temperature dependence of the
1726   deliquescence properties of hygroscopic aerosols, Atmos. Environ., 27, 467–473,
1727   https://doi.org/10.1016/0960-1686(93)90204-C, 1993.

1728   Tang, I.N. and Munkelwitz, H.R.: Simultaneous determination of refractive index and density
1729   of an evaporating aqueous solution droplet, Aerosol Sci. Technol., 15, 201–207,
1730   https://doi.org/10.1080/02786829108959527, 1991.

1731   Tang, I. N., Wong, W.T., Munkelwitz, H.R.: The relative importance of atmospheric sulfates
1732   and nitrates in visibility reduction, Atmos. Environ., 15, 2463–2471, 1981.

1733   Tanré, D., Bräon, F.M., Deuzä, J.L., Dubovik, O., Ducos, F., Franäois, P., Goloub, P.,
1734   Herman, M., Lifermann, A., Waquet, F.: Remote sensing of aerosols by using polarized,
1735   directional and spectral measurements within the A-Train: The PARASOL mission,
1736   Atmos. Meas. Tech., 4, 1383–1395, https://doi.org/10.5194/amt-4-1383-2011, 2011.

Todd, M.C., Washington, R., Martins, J.V., Dubovik, O., Lizcano, G., M'Bainayel, S., Engelstaedter, S.: Mineral dust emission from the Bodélé Depression nothern Chad, during BoDEx 2005, J. Geophys. Res. Atmos., 112, 1–12, https://doi.org/10.1029/2006JD007170, 2007.

Toon, O.B., Pollack, J.B., Khare, B.N.: The optical constants of several atmospheric aerosol species: ammmonium sulfate, aluminum oxide, and sodium chloride, J. Geophys. Res., 81, 5733–5748, 1976.

Triaud, A.H.M.J.: Earth observation data group: aerosol refractive index archive. http://eodg.atm.ox.ac.uk/ARIA/data?Minerals/Hematite/(Triaud_2005)/hematite_Triaud _2005.ri, 2005.

Tsekeri, A., Lopatin, A., Amiridis, V., Marinou, E., Igloffstein, J., Siomos, N., Solomos, S., Kokkalis, P., Engelmann, R., Baars, H., Gratsea, M., Raptis, P.I.: GARRLiC and LIRIC : strengths and limitations for the characterization of dust and marine particles along with their mixtures, Atmos. Meas. Tech., 10, 4995–5016, https://doi.org/10.5194/amt-10-4995-2017, 2017.

Usher, C. R., Michel, A. E., Grassian, V. H.: Reactions on mineral dust, Chem. Rev., 103, 4883-4939, https://doi.org/10.1021/cr020657y, 2003.

Voss, K.J., Morel, A., Antoine, D.: Detailed validation of the bidirectional effect in various Case 1 waters for application to ocean color imagery, Biogeosciences, 4, 781–789, https://doi.org/10.5194/bg-4-781-2007, 2007

Wagner, R., Ajtai, T., Kandler, K., Lieke, K., Linke, C., Müller, T., Schnaiter, M., and Vragel, M.: Complex refractive indices of Saharan dust samples at visible and near UV wavelengths: a laboratory study, Atmos. Chem. Phys., 12, 2491–2512, doi:10.5194/acp-12-2491-2012, 2012.

Wang, L., Li, Z., Tian, Q., Ma, Y., Zhang, F., Zhang, Y., Li, D., Li, K., Li, L. : Estimate of aerosol absorbing components of black carbon, brown carbon, and dust from ground-based remote sensing data of sun-sky radiometers, J. Geophys. Res. Atmos., 118, 6534–6543, https://doi.org/10.1002/jgrd.50356, 2013.

Wanner, W., Li, X., Strahler, A. : On the derivation of kernels for kernel-driven models of bidirectional reflectance, J. Geophys. Res., 100, 21077–21089, 1995.

Waquet, F., Cornet, C., Deuzé, J.L., Dubovik, O., Ducos, F., Goloub, P., Herman, M., Lapyonok, T., Labonnote, L.C., Riedi, J., Tanré, D., Thieuleux, F., Vanbauce, C.: Retrieval of aerosol microphysical and optical properties above liquid clouds from POLDER/PARASOL polarization measurements, Atmos. Meas. Tech., 6, 991–1016, https://doi.org/10.5194/amt-6-991-2013, 2013.

Washington, R., Todd, M., Middleton, N.J., Goudie, A.S.: Dust-storm source areas determined by the total ozone monitoring spectrometer and surface observations, Ann. Assoc. Am. Geogr., 93, 297–313, https://doi.org/10.1111/1467-8306.9302003, 2003.

Washington, R. and Todd, M.C.: Atmospheric controls on mineral dust emission from the Bodélé Depression, Chad: The role of the low level jet, Geophys. Res. Lett., 32, 1–5. https://doi.org/10.1029/2005GL023597, 2005.

Washington, R., Todd, M.C., Engelstaedter, S., Mbainayel, S., Mitchell, F.: Dust and the low-level circulation over the Bodélé Depression, Chad: Observations from BoDEx 2005, J. Geophys. Res. Atmos., 111, 1–15, https://doi.org/10.1029/2005JD006502, 2006.

Weber, R.J., Sullivan, A.P., Peltier, R.E., Russell, A., Yan, B., Zheng, M., de Grouw, J., Warneke, C., Brock, C., Holloway, J.S., Atlas, E.L., Edgerton, E.: A study of secondary organic aerosol formation in the anthropogenic-influenced southeastern United States, J. Geophys. Res. Atmos., 112, 1–13, https://doi.org/10.1029/2007JD008408, 2007.

Xie Y., Li Z., Li L. et al.: Study on influence of different mixing rules on the aerosol components retrieval from ground-based remote sensing measurements. Atmospheric Research, 145: 267-278, 2014.

Yu, H., Dickinson, R.E., Chin, M., Kaufman, Y.J., Holben, B.N., Geogdzhayev, I. V., Mishchenko, M.I.: Annual cycle of global distributions of aerosol optical depth from integration of MODIS retrievals and GOCART model simulations, J. Geophys. Res.

Atmos., 108, 1–14, https://doi.org/10.1029/2002JD002717, 2003

Yu, H., Dickinson, R.E., Chin, M., Kaufman, Y.J., Zhou, M., Zhou, L., Tian, Y., Dubovik, O., Holben, B.N.: Direct radiative effect of aerosols as determined from a combination of MODIS retrievals and GOCART simulations, J. Geophys. Res. Atmos., 109, 1–13, https://doi.org/10.1029/2003JD003914, 2004.

Yu, H., Kaufman, Y.J., Chin, M., Feingold, G., Remer, L.A., Anderson, T.L., Balkanski, Y., Bellouin, N., Boucher, O., Christopher, S., DeCola, P., Kahn, R., Koch, D., Loeb, N., Reddy, M.S., Schulz, M., Takemura, T., Zhou, M.: A review of measurement-based assessments of the aerosol direct radiative effect and forcing, Atmos. Chem. Phys., 6, 613–666, https://doi.org/10.5194/acp-6-613-2006, 2006.

Zhang, X. Y., Gong, S. L., Shen, Z. X., Mei, F. M., Xi, X. X., Liu, L. C., Zhou, Z. J., Wang, D., Wang, Y. Q., Cheng, Y.: Characterization of soil dust aerosol in China and its transport and distribution during 2001 ACE-Asia: 1. Network observations, J. Geophys. Res., 108 (D9), 4261, https://doi.org/4210.1029/2002JD002632, 2003.

Zhang, J., Reid, J.S., Westphal, D.L., Baker, N.L., Hyer, E.J.: A system for operational aerosol optical depth data assimilation over global oceans, J. Geophys. Res. Atmos., 113, 1–13, https://doi.org/10.1029/2007JD009065, 2008a.

Zhang, X.Y., Wang, Y.Q., Niu, T., Zhang, X.C., Gong, S.L., Zhang, Y.M., Sun, J.Y.: Atmospheric aerosol compositions in China: Spatial/temporal variability, chemical signature, regional haze distribution and comparisons with global aerosols, Atmos. Chem. Phys., 12, 779–799, https://doi.org/10.5194/acp-12-779-2012, 2012.

Zhang, X.Y., Wang, Y.Q., Wang, D., Gong, S.L., Arimoto, R., Mao, L.J., Li, J.: Characterization and sources of regional-scale transported carbonaceous and dust aerosols from different pathways in coastal and sandy land areas of China, J. Geophys. Res. Atmos., 110, 1–13, https://doi.org/10.1029/2004JD005457, 2005.

Zhang, X.Y., Wang, Y.Q., Zhang, X.C., Guo, W., Gong, S.L.: Carbonaceous aerosol composition over various regions of China during 2006, J. Geophys. Res. Atmos., 113, 1–10, https://doi.org/10.1029/2007JD009525, 2008b.

Tables

Table 1. List of measured and retrieved characteristic considered in POLDER/GRASP with aerosol component mixing model. $\mu_0 = cos(\vartheta_0)$ depends on the solar zenith angle ϑ_0, $\mu_1 = cos(\vartheta_1)$ depends on the observation zenith angle ϑ_1. φ_0 and φ_1 represent the solar and observation azimuth angles.

POLDER/PARASOL measurements	
Measurements type:	
$I(\mu_0; \mu_1; \varphi_0; \varphi_1; \lambda_i) = I(\Theta_j; \lambda_i)$	– I reflected total radiances
$Q(\mu_0; \mu_1; \varphi_0; \varphi_1; \lambda_i) = Q(\Theta_j; \lambda_i)$	– Q component of the Stokes vector
$U(\mu_0; \mu_1; \varphi_0; \varphi_1; \lambda_i) = U(\Theta_j; \lambda_i)$	– U component of the Stokes vector
Observation specifications:	
Angular:	
	$I(\Theta_j; \lambda_i)$, $Q(\Theta_j; \lambda_i)$ and $U(\Theta_j; \lambda_i)$ measured in up to 16 viewing directions, that may cover the range of scattering angle Θ from ~ 80° to 180°
Spectral:	
	$I(\Theta_j; \lambda_i)$ measured in 6 window channels λ_i = 0.440, 0.490, 0.565, 0.670, 0.865 and 1.02 μm
	$Q(\Theta_j; \lambda_i)$ and $U(\Theta_j; \lambda_i)$ measured in 3 window channels λ_i = 0.490, 0.670, and 0.865 μm
Retrieved characteristic	
Aerosol parameters:	
C_v	– total volume concentration of aerosol ($\mu m^3/\mu m^2$)
$dV(r_i)/dlnr$	– ($i = 1, ..., N_r$) values of volume size distribution in N_i size bins r_i normalized by C_v
C_{sph}	– fraction of spherical particles
h_0	– mean height of aerosol layer
$Frac(F_i)$	– ($i = 1, ..., N_f$) the fraction of component in fine mode
$Frac(C_i)$	– ($i = 1, ..., N_c$) the fraction of component in coarse mode
Surface reflection parameters:	
Ross-Li model parameters:	
$k_{iso}(\lambda_i)$	– ($i = 1, ..., N_\lambda = 6$) first Ross-Li model parameter (isotropic parameter characterizing isotropic surface reflectance)
$k_{vol}(\lambda_i)$	– ($i = 1, ..., N_\lambda = 6$) second Ross-Li model parameter (volumetric parameter characterizing anisotropy of reflectance)
$k_{geom}(\lambda_i)$	– ($i = 1, ..., N_\lambda = 6$) third Ross-Li model parameter (geometric parameter characterizing anisotropy of reflectance)
Maignan et al. (2009) model:	
$B(\lambda_i)$	– ($i = 1, ..., N_\lambda = 6$) free parameter

1859   **Table 2.** Description of aerosol components and complex refractive indices at 0.440

1860 μm and 0.865 μm employed in the GRASP components retrieval approach, as well as

1861   those used in the uncertainty tests.

Abb.	Component	Complex refractive index		Reference
		0.440 μm	0.865 μm	
BC	Black carbon representing wavelength-independent strong absorption	1.95+0.79i	1.95+0.79i	Bond & Bergstrom (2006)
		1.75+0.63i	1.75+0.63i	Bond & Bergstrom (2006)
BrC	Brown carbon representing wavelength-dependent absorption	1.54+0.07i	1.54+0.003i	Sun et al. (2007)
		1.54+0.06i	1.54+0.0005i	Kirchstetter et al. (2004)
FNAI	Fine mode non-absorbing insoluble representing fine non-absorbing dust and organic carbon	1.54+0.0005i	1.52+0.0005i	Ghosh (1999)
		1.53+0.005i	1.53+0.005i	"GKI"[1]
		1.52+0.0006i	1.50+0.0006i	Koepke et al. (1997)
FNAS	Fine mode non-absorbing soluble representing inorganic salts	$1.337+10^{-9}$i	$1.339+10^{-8}$i	Tang et al. (1981); Gosse et al. (1997) for "AN"[2]
		$1.537+10^{-7}$i	$1.517+10^{-7}$i	Toon et al. (1976) for "AS" [3]
FAWC	Fine mode aerosol water content	$1.337+10^{-9}$i	$1.329+10^{-6.5}$i	Hale & Querry (1973)
CAI	Coarse mode absorbing insoluble representing iron oxides	2.90+0.345i	2.75+0.003i	Longtin et al. (1988)
		2.88+0.987i	2.72+0.140i	Triaud (2005)
CNAI	Coarse mode non-absorbing insoluble represented by non-absorbing dust	1.54+0.0005i	1.52+0.0005i	Ghosh (1999)
		1.53+0.005i	1.53+0.005i	"GKI"[1]
CNAI	by Organic Carbon	1.52+0.0006i	1.50+0.0006i	Koepke et al. (1997)
CNAS	Coarse mode non-absorbing soluble represented by an inorganic salt - AN[2]	$1.337+10^{-9}$i	$1.339+10^{-8}$i	Tang et al. (1981); Gosse et al. (1997)
CNAS	by AS[3]	$1.537+10^{-7}$i	$1.517+10^{-7}$i	Toon et al. (1976)
CAWC	Coarse mode aerosol water content	$1.337+10^{-9}$i	$1.329+10^{-6.5}$i	Hale & Querry (1973)

1862   "GKI"[1] denotes dust composed of a mixture of quartz (Ghosh, 1999), kaolinite (Sokolik and

1863   Toon, 1999) and illite (Sokolik and Toon, 1999) with the proportions recalculated from

1864   Journet et al. (2014).

1865   "AN"[2] denotes ammonium nitrate, which can be used to create a host in aerosols.

1866   "AS"[3] denotes ammonium sulfate, which is an alternative species for the host estimation in

1867   aerosols.

1868
1869
1870
1871
1872
1873
1874
1875
1876
1877
1878
1879
1880
1881
1882
1883
1884

Table 3. List of statistics for parameters between assumed and retrieved in the sensitivity tests of GRASP component retrieval using Maxwell-Garnett mixing model. The values of slope (A), intercept (B), correlation coefficient (R), root-mean-square error (RMSE), mean absolute error (MAE), mean relative error (MRE) and standard error deviation (STD) are presented for aerosol components, aerosol optical thickness (AOT), Single-scattering albedo (SSA), real (n) and imaginary (k) parts of complex refractive index in fine mode (FM) and coarse mode (CM) at 675 nm.

	A	B	R	RMSE	MAE	MRE	STD
BC	1.00	0.00	1.00	0.00	0.00	0.4%	0.00
BrC	1.00	0.00	1.00	0.00	0.00	2.7%	0.00
FNAI	1.02	-0.02	0.99	0.03	-0.01	-1.0%	0.03
FNAS	1.03	-0.03	1.00	0.01	-0.02	-6.0%	0.01
FAWC	0.99	0.00	1.00	0.02	0.00	-0.2%	0.02
RH	0.94	0.04	0.97	0.03	0.00	0.3%	0.03
CAI	1.00	0.00	1.00	0.00	0.00	-1.1%	0.00
CNAI	0.95	0.01	0.99	0.02	0.00	8.2%	0.02
CNAS	0.95	0.00	1.00	0.01	-0.02	-4.5%	0.01
CAWC	1.01	0.00	1.00	0.02	0.00	0.9%	0.02
AOT	1.00	0.00	1.00	0.00	0.00	0.0%	0.00
SSA	1.00	0.00	1.00	0.00	0.00	0.0%	0.00
FM(n)	0.98	0.03	1.00	0.00	0.00	0.1%	0.00
FM(k)	1.00	0.00	1.00	0.0003	0.0001	0.5%	0.00
CM(n)	1.00	0.00	1.00	0.00	0.00	0.0%	0.00
CM(k)	0.96	0.00	1.00	0.0000	0.0000	5.8%	0.00

1920 **Table 4.** The statistics of aerosol parameters in Fig. 10: number of measurements (N), slope
1921 (A), intercept (B), correlation coefficient (R), root-mean-square error (RMSE), mean absolute
1922 error (MAE), standard error deviation (STD). GRASP approach (GA): Maxwell-Garnett
1923 (MG) mixing model, volume-weighted (VW) mixing model; standard (ST)
1924 GRASP/PARASOL retrievals without aerosol component mixing model.
1925

	Banizoumbou AOT (675 nm)			Tamanrasset AOT (675 nm)			Mongu AOT (675 nm)		
N	78			76			118		
GA	MG	VW	ST	MG	VW	ST	MG	VW	ST
A	0.75	0.96	0.68	0.68	0.88	0.49	0.90	0.96	0.96
B	-0.02	-0.05	0.08	0.03	0.06	0.13	-0.01	0.00	0.00
R	0.97	0.96	0.91	0.89	0.88	0.51	0.96	0.95	0.94
RMSE	0.08	0.11	0.13	0.05	0.07	0.12	0.04	0.05	0.06
MAE	-0.15	-0.07	-0.08	-0.02	0.04	0.05	-0.04	-0.01	-0.01
STD	0.13	0.11	0.19	0.07	0.07	0.14	0.05	0.05	0.06

	Skukuza AOT (675 nm)			Solar village AOT (675 nm)			Agoufou AOT (675 nm)		
N	92			98			117		
GA	MG	VW	ST	MG	VW	ST	MG	VW	ST
A	0.83	0.96	0.89	0.75	0.83	0.67	0.83	0.98	0.72
B	-0.01	0.00	0.01	0.00	0.02	0.10	0.00	0.00	0.20
R	0.79	0.76	0.84	0.91	0.91	0.79	0.94	0.94	0.84
RMSE	0.05	0.06	0.04	0.09	0.10	0.13	0.14	0.16	0.21
MAE	-0.03	-0.01	-0.01	-0.11	-0.06	-0.05	-0.10	-0.01	0.04
STD	0.05	0.06	0.04	0.11	0.11	0.16	0.16	0.16	0.25

	All sites AOT (675 nm)			All sites AE (870/440)			All sites SSA (675 nm)		
N	579			429			101		
GA	MG	VW	ST	MG	VW	ST	MG	VW	ST
A	0.79	0.93	0.77	0.86	0.79	0.88	0.57	0.59	0.65
B	0.00	0.00	0.07	0.20	0.17	0.16	0.44	0.42	0.32
R	0.95	0.95	0.88	0.93	0.92	0.94	0.83	0.84	0.77
RMSE	0.09	0.11	0.15	0.24	0.24	0.24	0.02	0.02	0.03
MAE	-0.07	-0.02	-0.01	0.08	0.00	0.06	0.04	0.04	0.00
STD	0.11	0.11	0.17	0.26	0.29	0.25	0.03	0.03	0.04

1934
1935
1936
1937 **Figures**
1938
1939
1940
1941
1942
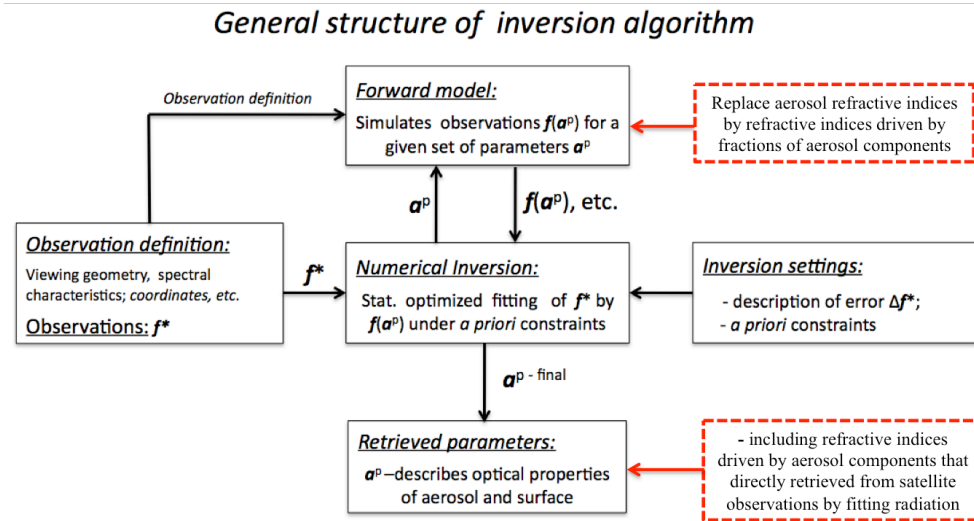
1943
1944 **Figure 1.** The general structure of GRASP algorithm with aerosol component conversion
1945 model, courtesy of (Dubovik et al., 2011). The red dashed frames represent modifications
1946 for the component inversion approach. f^* represents vector of inverted measurements, a^P
1947 represents vector of unknowns at the p-th iteration, $f(a^P)$ represents vector of measurement
1948 fit at the p-th iteration.
1949
1950
1951
1952
1953
1954
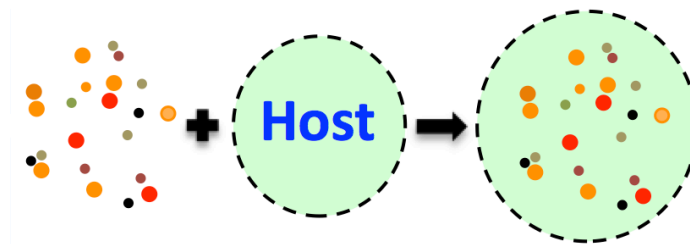
1955
1956 **Figure 2.** Illustrates a general logistics of an effective refractive index calculation using a
1957 conversion model that is based upon the Maxwell-Garnett effective medium approximation.
1958
1959
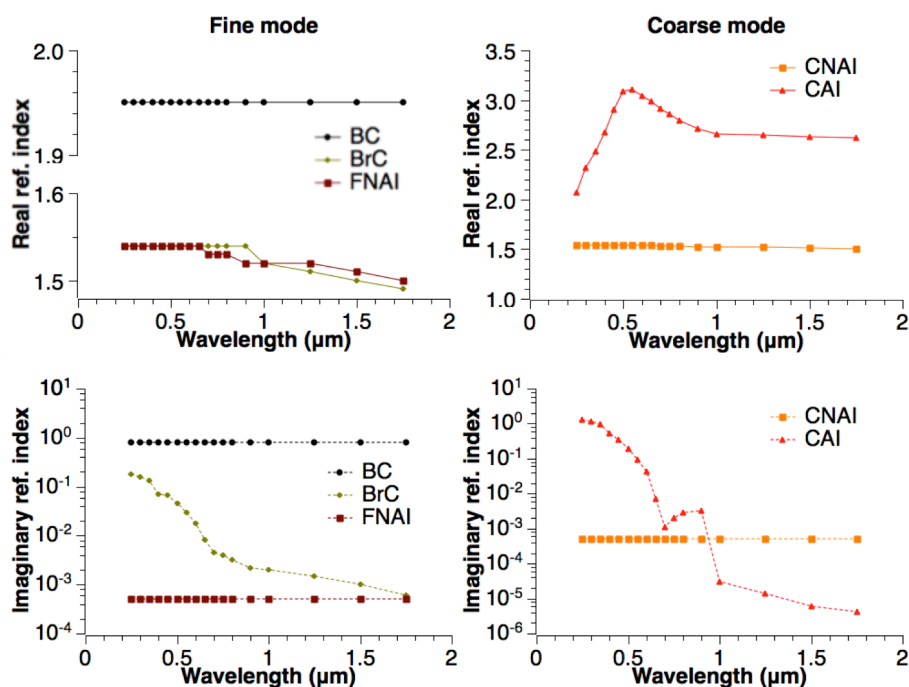
Figure 3. The refractive indices of assumed aerosol components embedded in the host of the size-dependent Maxwell-Garnett conversion model. The parameters of BC refer to Bond and Bergstrom (2006). The parameters of BrC refer to Sun et al. (2007) and Schuster et al. (2016a). The parameters of fine non-absorbing insoluble (FNAI) and coarse non-absorbing insoluble (CNAI) refer to Ghosh (1999). FNAI represents dust and OC in fine mode particles, while CNAI represents dust in coarse mode particles. The parameters of coarse absorbing insoluble (CAI) refer to Longtin et al. (1988) representing hematite.
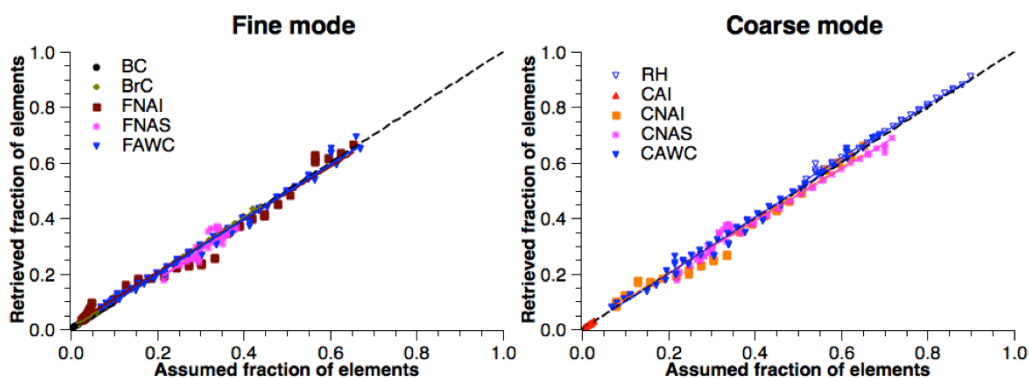
Figure 4. Assumed and retrieved fractions of aerosol species resulting from the sensitivity tests of GRASP/Component retrieval using Maxwell-Garnett mixing model.
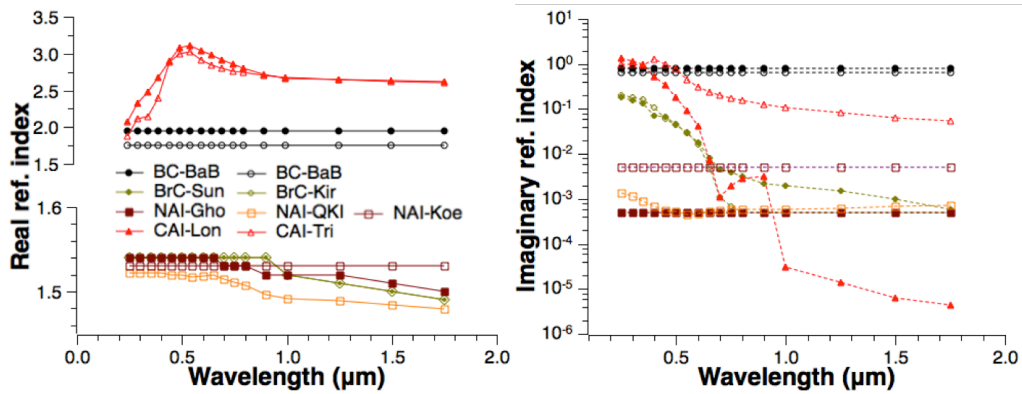
1979
1980 **Figure 5**. Complex refractive index of several aerosol species (BC, BrC, CAI, and NAI) in
1981 the host. The values with filled symbols are used in the presented size-dependent Maxwell-
1982 Garnett conversion model. The values with open symbols are used to replace the
1983 corresponding values to test the uncertainties in the aerosol component retrievals. "BaB" for
1984 Bond and Bergstrom (2006); "Sun" for Sun et al. (2007); "Kir" for Kirchstetter et al. (2004);
1985 "Gho" for Ghosh (1999); "QKI" for dust composed of a mixture of quartz (Ghosh, 1999),
1986 kaolinite (Sokolik and Toon, 1999) and illite (Sokolik and Toon, 1999) with the proportions
1987 of 48%, 26%, and 26%, respectively (Journet et al., 2014); "Koe" for Koepke et al. (1997);
1988 "Lon" for Longtin et al. (1988); and "Tri" for Triaud (2005).

1989
1990
1991
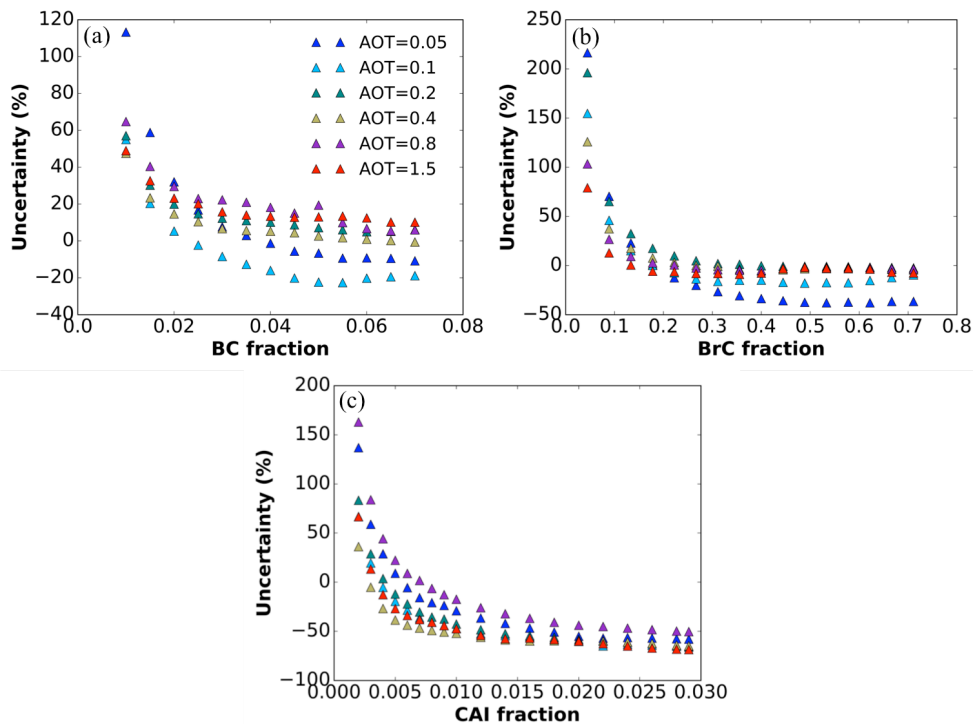
1992
1993 **Figure 6.** Uncertainty in absorbing species retrievals from POLDER/PARASOL attributed to
1994 the refractive index variability; uncertainties in (a) BC, (b) BrC, and (c) CAI fractions.

1995
1996
1997
1998
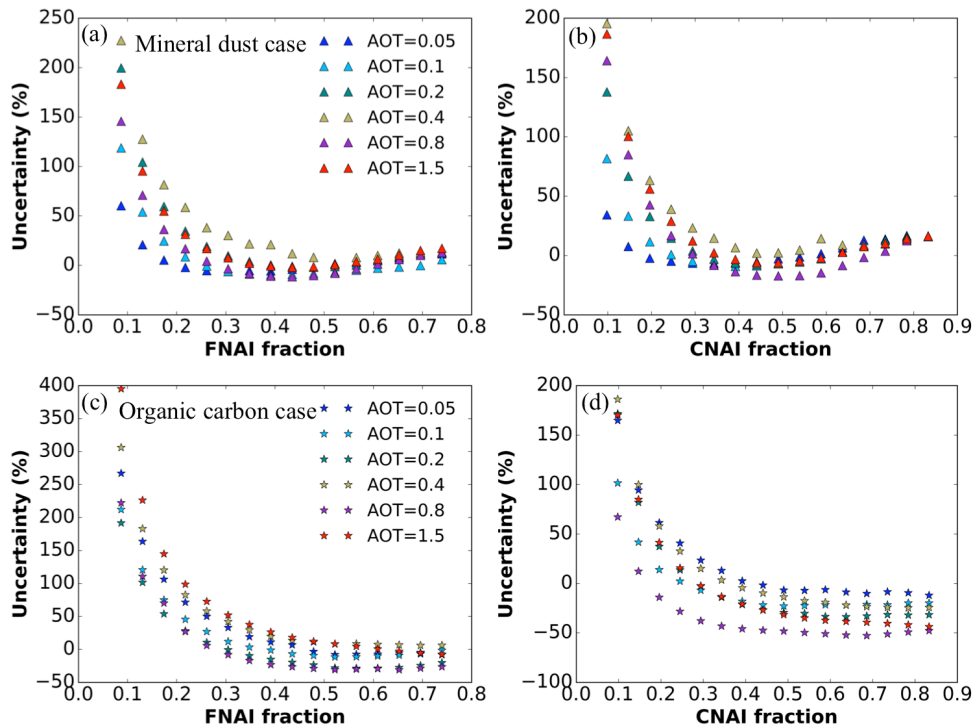
1999
2000
2001 **Figure 7.** Uncertainty in Non-Absorbing Insoluble particles fraction in Fine (FNAI) and
2002 Coarse (CNAI) modes attributed to the refractive index variability: (a), (b) for the case of
2003 mineral dust and (c), (d) for organic carbon.
2004
2005
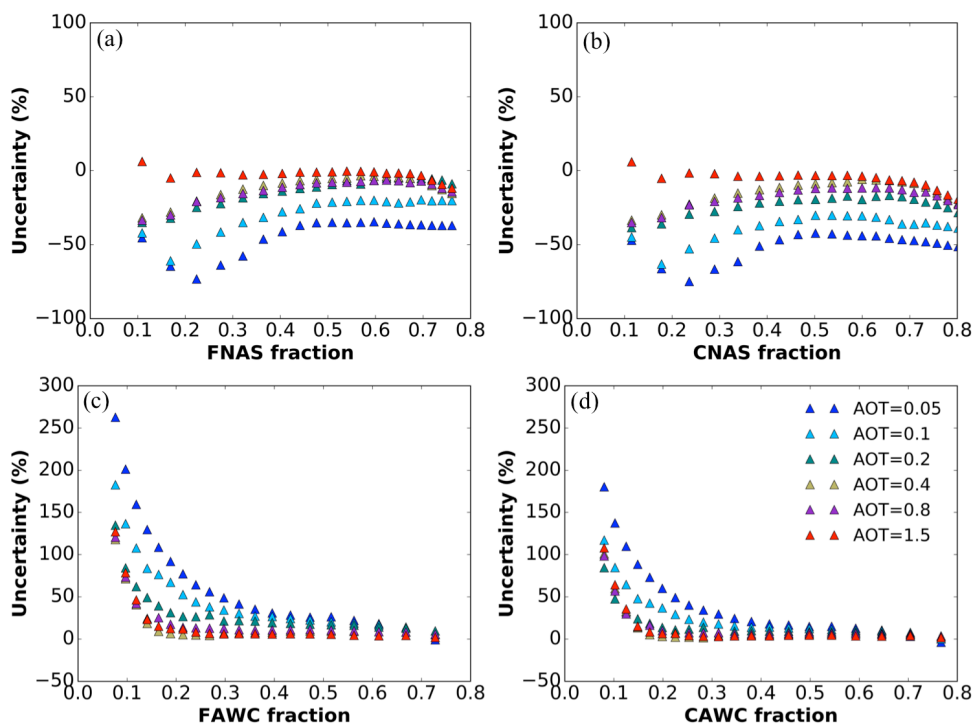
2006
2007 **Figure 8.** Uncertainty in Non-Absorbing Soluble particles and aerosol water content fraction
2008 in Fine (FNAS, FAWC) and Coarse (CNAS, CAWC) modes attributed to the refractive index
2009 and hygroscopic properties of ammonium nitrate and ammonium sulfate.
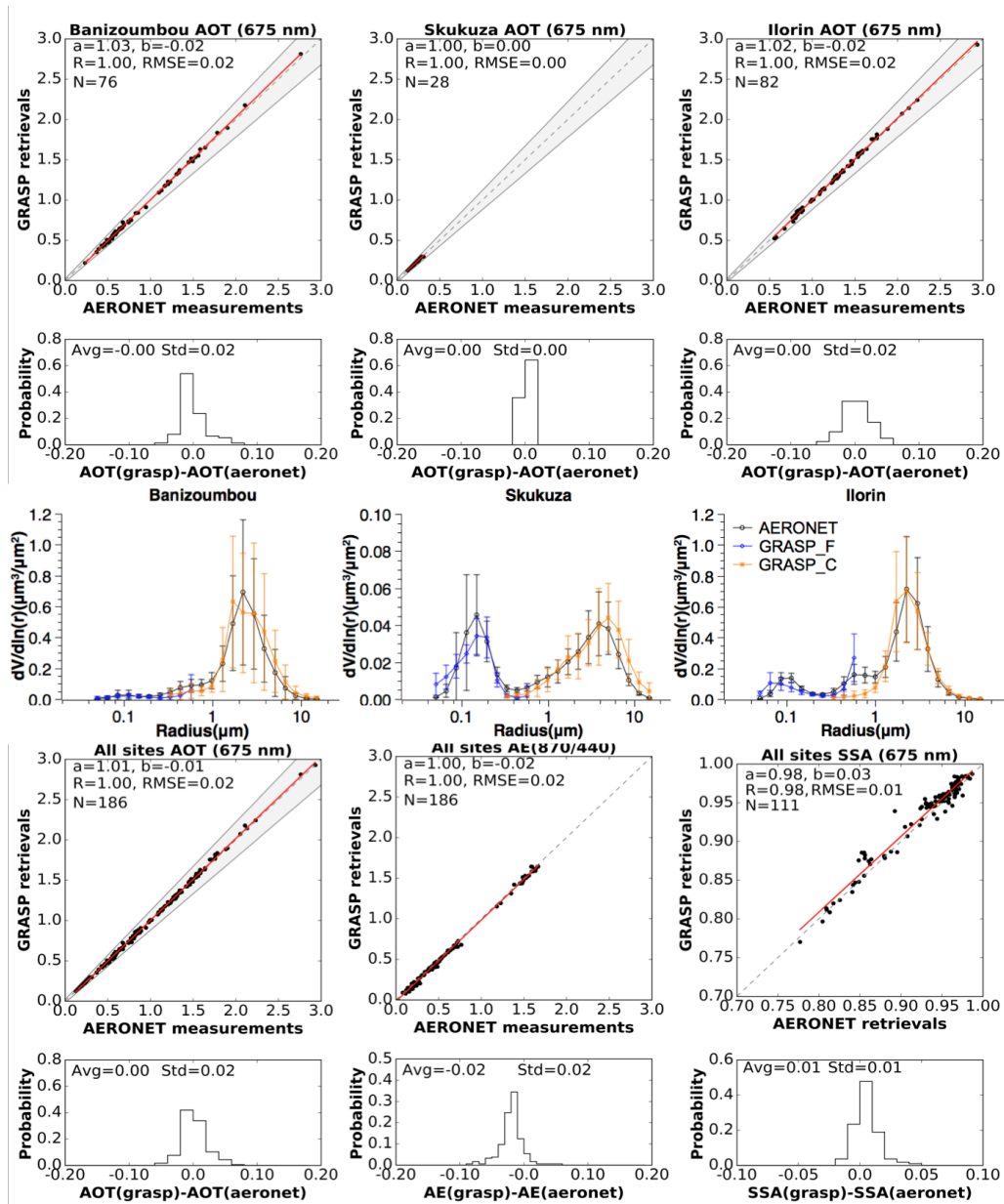
Figure 9. The inter-comparison of aerosol optical properties derived from Sun/sky photometer measurements using the GRASP/Component approach with the corresponding values of the AERONET operational product. The data presented for the Banizoumbou site in April 2007 represent mineral dust aerosol, for the Skukuza site in September 2007 represent the biomass burning aerosol, and for the Ilorin site in January 2007 represent the mixture of dust and biomass burning.
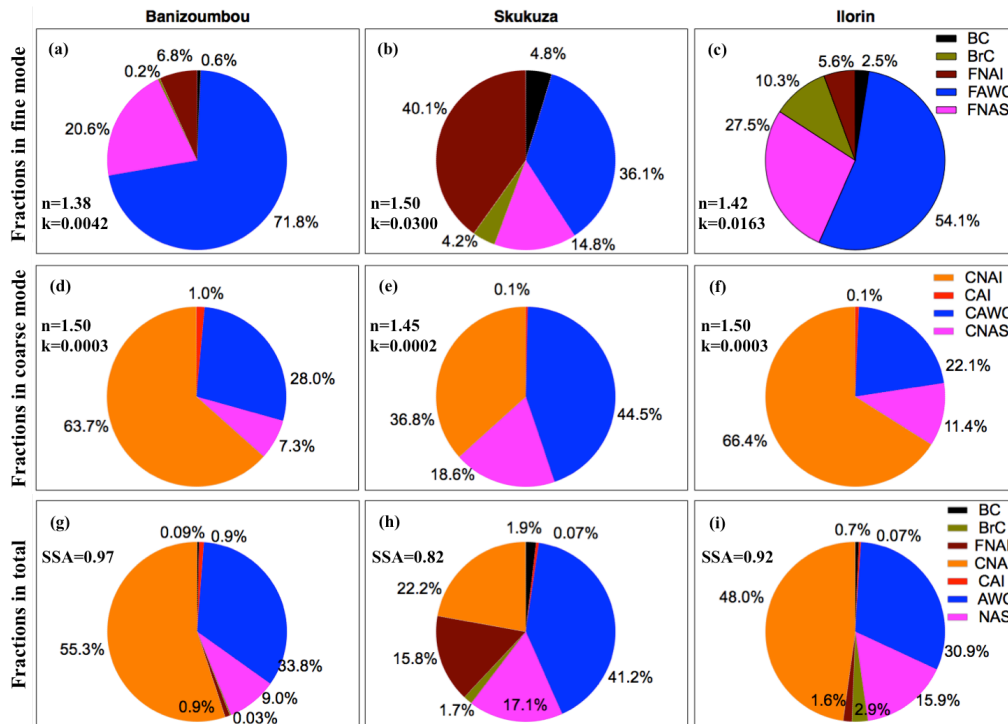
Figure 10. Examples of aerosol component retrievals derived from AERONET Sun/sky photometer measurements using the GRASP/Component approach. Panels: (a, d, g) the mineral dust case at the Banizoumbou site (April 8th, 2007); (b, e, h) the biomass burning case at the Skukuza site (September 2nd, 2007); and (c, f, i) the mixture of dust and biomass burning at the Ilorin site (January 25th, 2007). In the panes are also indicated the values of complex refractive index (n, k) at 675 nm retrieved for the fine and coarse modes, and of SSA at 675 nm derived for ensemble of aerosol.
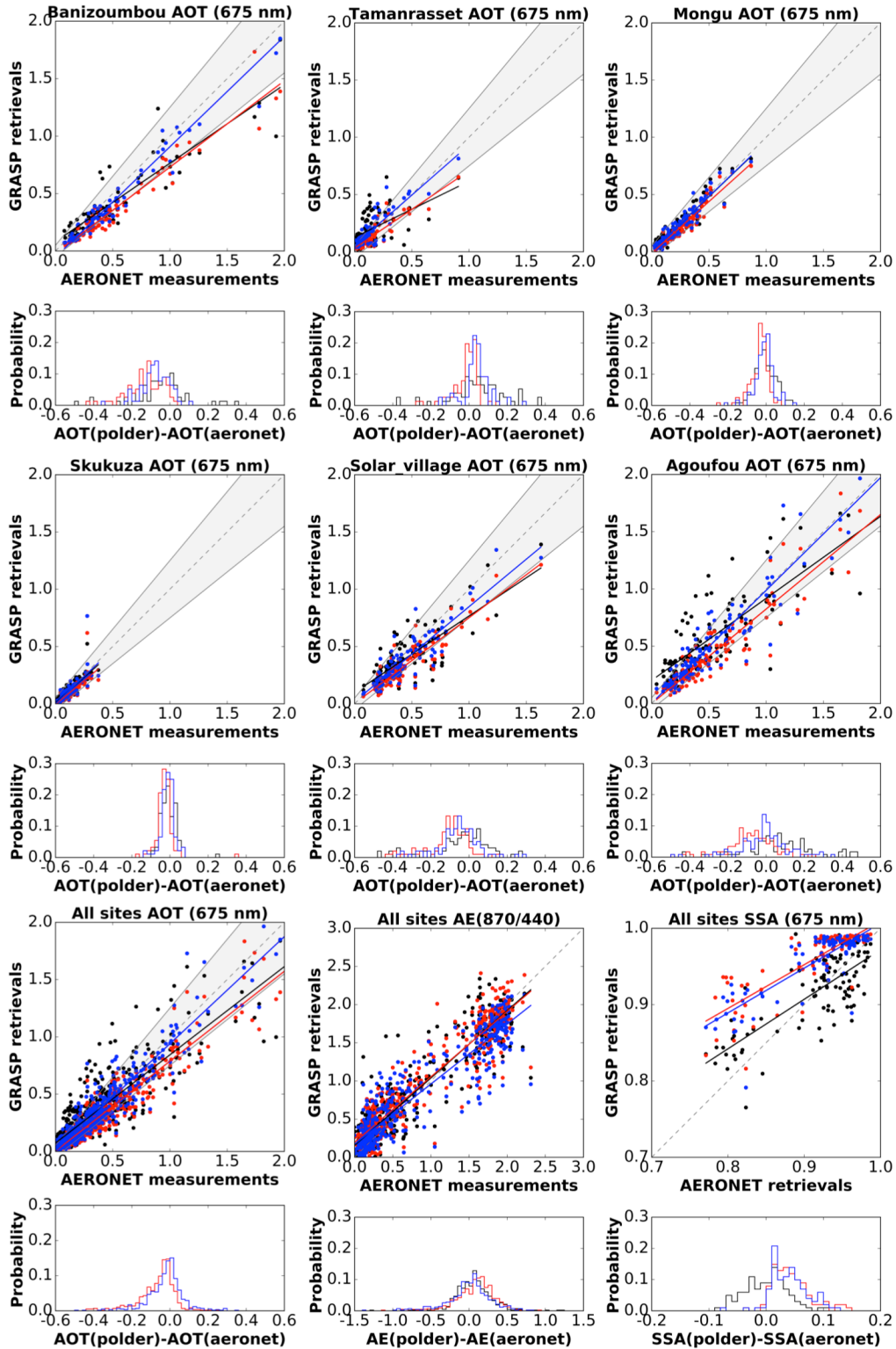
Figure 11. Inter-comparison of aerosol optical properties retrieved from POLDER/PARASOL and provided by AERONET operational product in six AERONET sites located in Africa and Middle East during the period 2006 to 2008. Red color represents the Maxwell-Garnett (MG) mixing model; blue color represents the volume-weighted (VW) mixing model; and black color represents the standard (ST) GRASP/PARASOL product that do not employ the aerosol component retrievals.

2042
2043
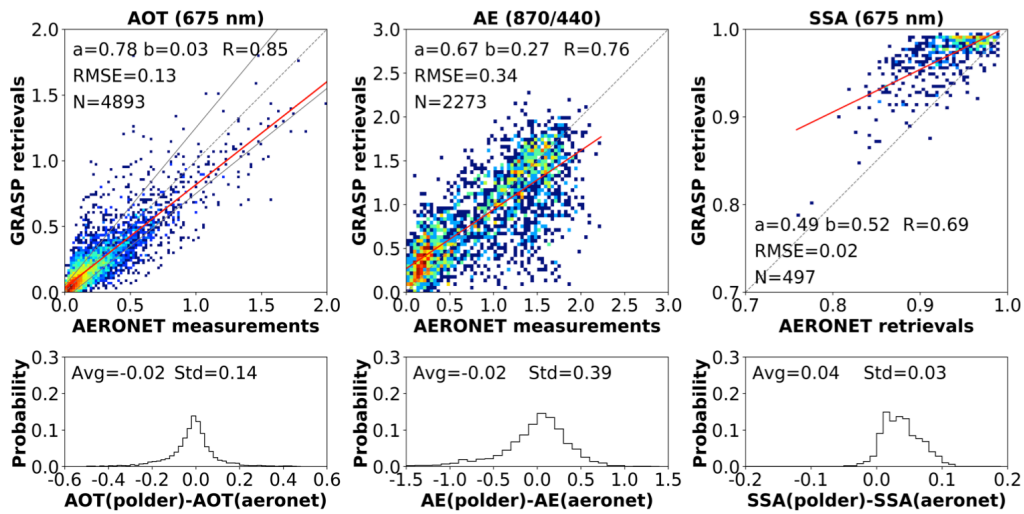
2044
2045 **Figure 12.** Inter-comparison of aerosol optical properties retrieved using the
2046 POLDER/PARASOL component (MG mixing model) approach and the corresponding
2047 operational AERONET products from all globally available sites in 2008.

2048

2049
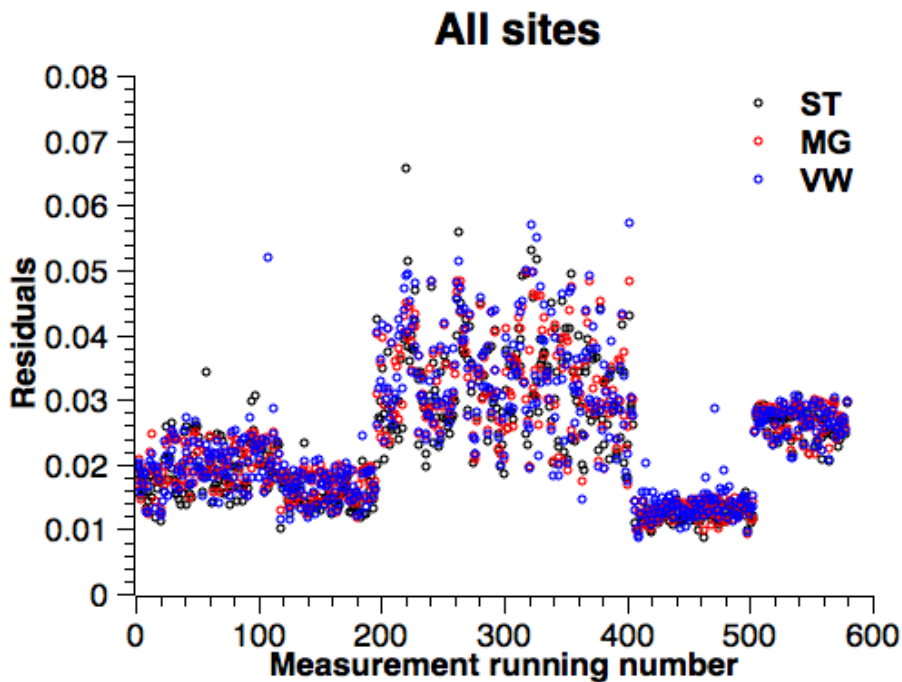
2050

2051 **Figure 13.** Inter-comparison of retrieval residuals among different GRASP approaches. Red
2052 color represents the Maxwell-Garnett (MG) mixing model; blue represents the volume-
2053 weighted (VW) mixing model; and black represents the standard (ST) GRASP/PARASOL
2054 product that do not employ the aerosol component retrievals.

2055

2056

2057

2058

2059

2060

2061

Figure 14. Seasonal variability of number of pixels in 0.1×0.1 degree resolution observed by POLDER/PARASOL satellite over the globe in 2008.
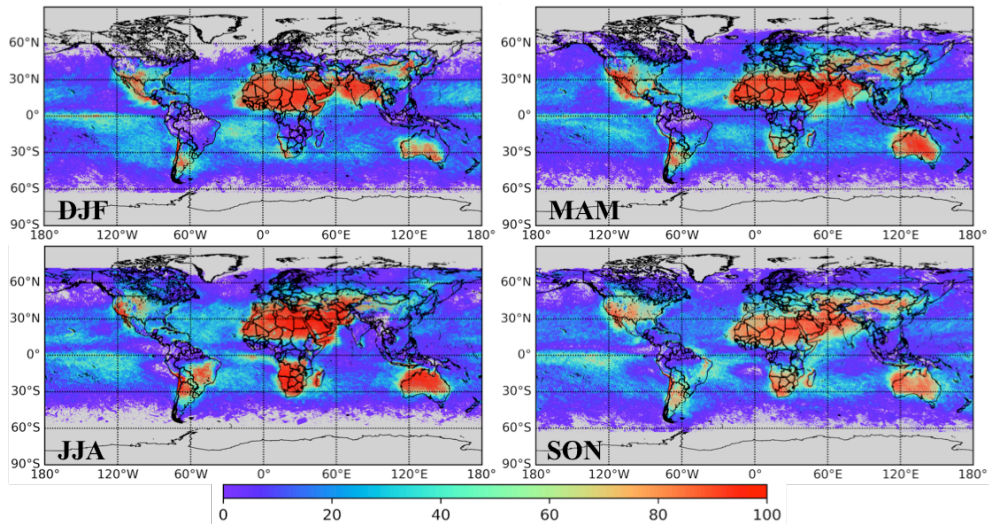
2065
2066
2067
2068
2069
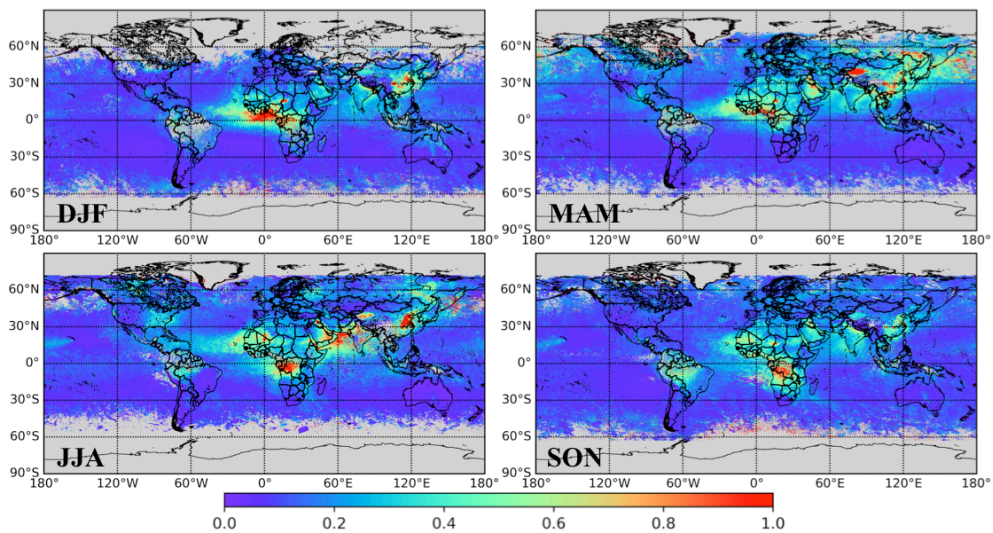
Figure 15. Seasonal variability of AOT at 565 nm in 2008 as retrieved by GRASP/Component algorithm from POLDER/PARASOL satellite observations.

2074
2075

2076
2077
2078

2079
2080 **Figure 16.** Seasonal variability of BC column volume concentration (mm^3/m^2) over the globe
2081 in 2008 as retrieved by GRASP/Component algorithm from POLDER/PARASOL satellite
2082 observations.
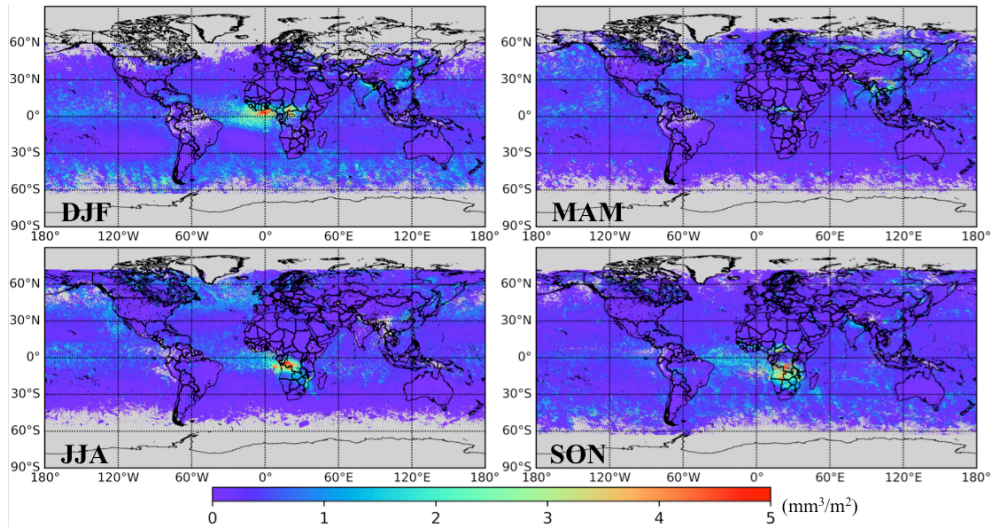
2083
2084
2085
2086
2087
2088

2089
2090 **Figure 17.** Same as Fig. 16, but for BrC
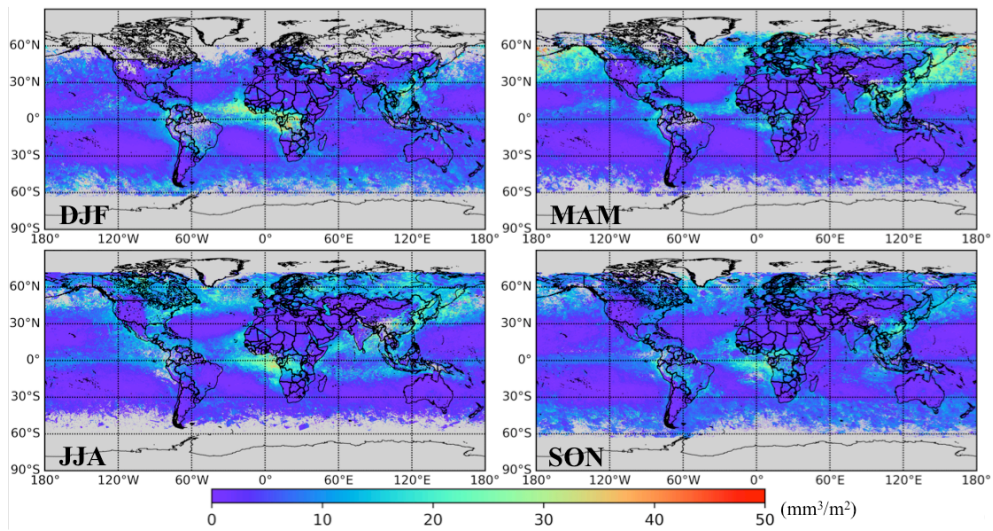
2091
2092
2093
2094
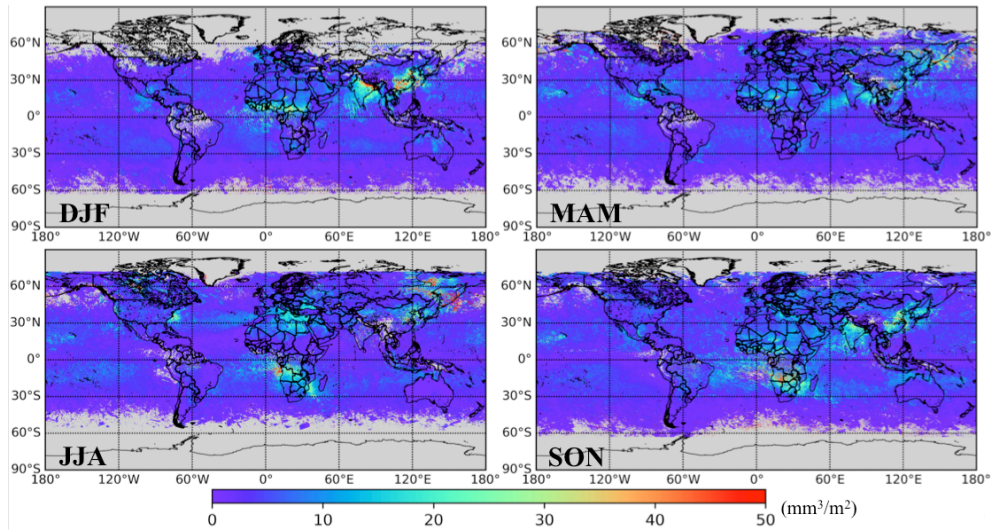
Figure 18. Same as Fig. 16, but for fine mode non-absorbing soluble (FNAS)
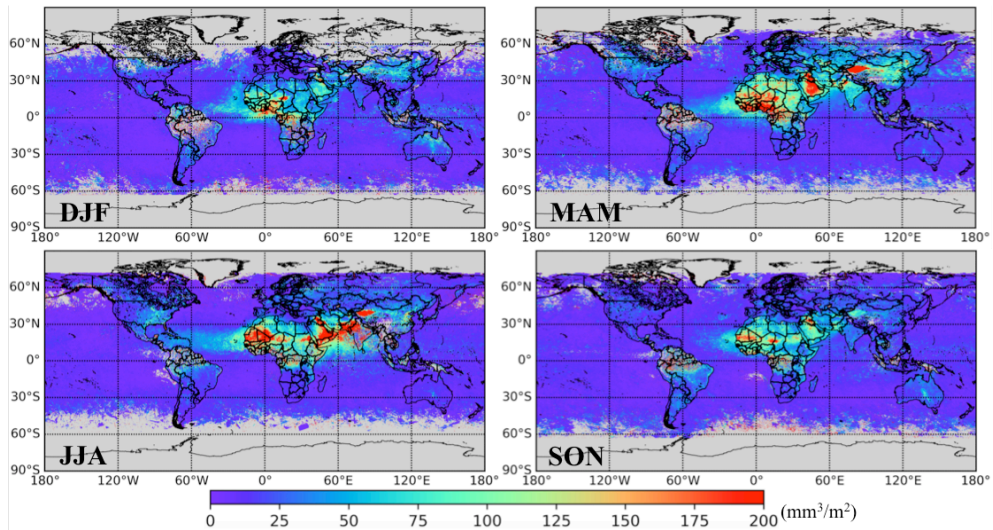
Figure 19. Same as Fig. 16, but for coarse mode non-absorbing insoluble (CNAI, dust)
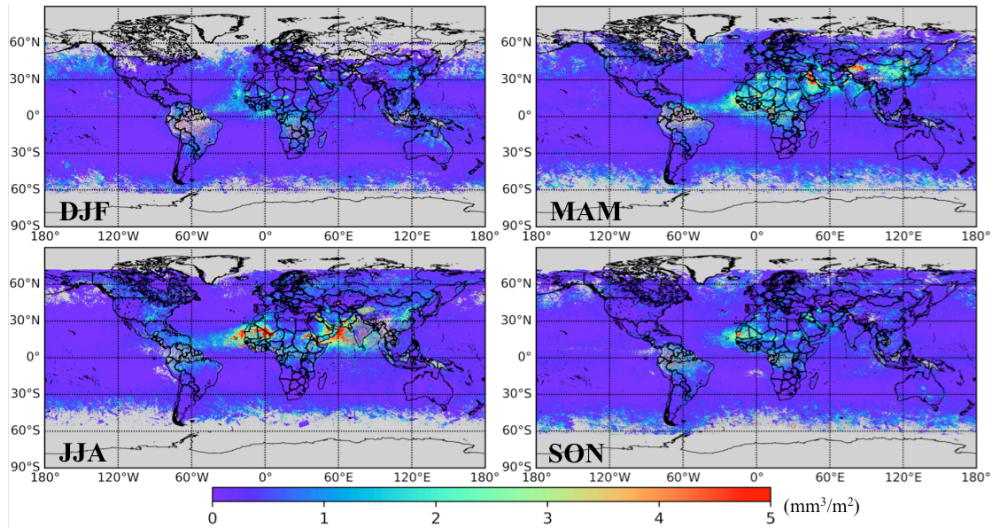
Figure 20. Same as Fig. 16, but for coarse mode absorbing insoluble (CAI, FeOx and Carbonaceous particles)
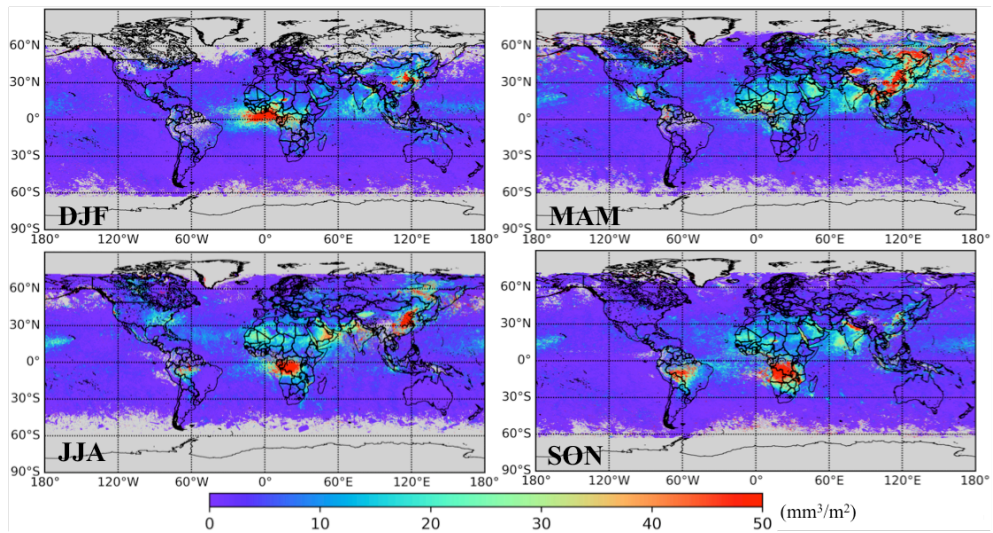
Figure 21. Same as Fig. 16, but for fine mode non-absorbing insoluble (FNAI, dust and OC)